Progress in Biophysics and Molecular Biology 130 (2017) 150–169

Contents lists available at ScienceDirect

Progress in Biophysics and Molecular Biology

journal homepage: www.elsevier.com/locate/pbiomolbio

Electromechanical optical mapping

J. Christoph [a, b, *, 1], J. Schröder-Schetelig [a, c, 1], S. Luther [a, b, c, d, **]

[a] Max Planck Institute for Dynamics and Self-Organization, Am Fassberg 17, 37077 Göttingen, Germany
[b] German Center for Cardiovascular Research, Partner Site Göttingen, Germany
[c] University of Goettingen, Institute for Nonlinear Dynamics, Göttingen, Germany
[d] University Medical Center Goettingen, Institute of Pharmacology, Göttingen, Germany

ARTICLE INFO

Article history:
Received 14 March 2017
Accepted 10 September 2017
Available online 22 September 2017

Keywords:
Optical mapping
Cardiac fibrillation
Excitation-contraction coupling
Image registration
Motion artifact
Motion tracking

ABSTRACT

Optical mapping is a widely used imaging technique for investigating cardiac electrophysiology in intact, Langendorff-perfused hearts. Mechanical contraction of cardiac tissue, however, may result in severe motion artifacts and significant distortion of the fluorescence signals. Therefore, pharmacological uncoupling is widely used to reduce tissue motion. Recently, various image processing algorithms have been proposed to reduce motion artifacts. We will review these technological developments. Furthermore, we will present a novel approach for the three-dimensional, marker-free reconstruction of contracting Langendorff-perfused intact hearts under physiological conditions. The algorithm allows disentangling the fluorescence signals (e.g. membrane voltage or intracellular calcium) from the mechanical motion (e.g. tissue strain). We will discuss the algorithms reconstruction accuracy, resolution, and robustness using experimental data from Langendorff-perfused rabbit hearts.

1. Introduction

Fluorescence imaging techniques are widely used in the biophysical sciences to visualize electrophysiological processes in cells and tissues. In basic cardiological research, fluorescence imaging is referred to as *optical mapping* when used to study the propagation of electrical excitation in the heart (Salama and Morad, 1976; Morad and Salama, 1979; Salama et al., 1987). Optical mapping provides high-resolution visualizations of electro-chemical wave phenomena such as membrane potential or calcium waves evolving rapidly across the heart surface (Efimov et al., 1994; Choi and Salama, 2000). Providing maps of vortex wave dynamics during heart rhythm disorders such as ventricular fibrillation, the imaging technique has had a tremendous impact on the understanding of cardiac arrhythmias (Davidenko et al., 1992; Pertsov et al., 1993; Jalife and Gray, 1996; Gray et al., 1998; Witkowski et al., 1998). Today, optical mapping is recognized as the gold-standard imaging technique in the field. Optical mapping has been used to image normal and abnormal activity in intact hearts, wedge preparations of ventricles and atria, papillary muscle and cell culture preparations. Optical mapping has been performed in various species including excised human hearts (Nanthakumar et al., 2007). With modern multi-camera imaging setups, it is possible to image the entire surface of a heart using two or more cameras and to create panoramic maps representing the activity on the shape of the outer epicardial surface using calibrated cameras and techniques for the reconstruction of the three-dimensional heart geometry (Kay et al., 2004; Rogers et al., 2007; Qu et al., 2007).

One of the major shortcomings of optical mapping, as it is presently most commonly conducted, however, is its sensitivity to motion. Even the slightest motion can cause severe motion artifacts. These artifacts superimpose the wave patterns appearing in the optical maps and can prohibit further analysis of the imaging data. As a result, isolated hearts and other heart tissue preparations are typically imaged under ostensibly unphysiological conditions: any contractile motion or beating of the tissue is being suppressed using pharmacological excitation-contraction uncoupling agents. Nevertheless, it has been shown that motion does not constitute a fundamental limitation of optical mapping. Recent advancements of optical mapping indicated that undesired effects caused by motion can be efficiently reduced by applying numerical computer vision techniques, tracking the motion and stabilizing the image data. In this regard, several algorithms for post-acquisition motion artifact removal have been introduced, see section 1.3. Despite significant progress in the field, however, optical mapping of contracting hearts using numerical motion-compensation algorithms is not yet

* Corresponding author. Max Planck Institute for Dynamics and Self-Organization, Am Fassberg 17, 37077 Göttingen, Germany.
** Corresponding author. Max Planck Institute for Dynamics and Self-Organization, Am Fassberg 17, 37077 Göttingen, Germany..
E-mail addresses: jan.christoph@ds.mpg.de (J. Christoph), j.schroeder-schetelig@ds.mpg.de (J. Schröder-Schetelig), stefan.luther@ds.mpg.de (S. Luther).
URL: http://www.bmp.ds.mpg.de
[1] Both authors contributed equally.

https://doi.org/10.1016/j.pbiomolbio.2017.09.015

commonly used. Being able to perform optical mapping studies with beating hearts or other contracting cardiac tissue preparations is a highly desired objective in basic cardiac research. Measurements that could directly relate electrical and mechanical function of the heart would provide invaluable information about the mechanisms underlying cardiac disease and heart rhythm disorders.

Here, we discuss the problem of motion artifacts emerging in optical mapping recordings of contracting hearts. We discuss concepts to significantly reduce motion artifacts and review the current advances in the field. We also present a novel three-dimensional motion tracking method and data obtained in an optical mapping study with isolated beating rabbit hearts, showing action potential wave propagation across the three-dimensional deforming surface of the contracting ventricular wall.

1.1. Optical mapping

Optical mapping combines fluorescence imaging techniques and computational post-processing, creating optical filtering-mediated signals, which relate directly to electrophysiological processes. One of the most essential components of optical mapping is that the optical signals need to be amplified numerically before maps of impulse propagation or wave patterns can be visualized, see Fig. 1. In particular, the adaptation of computer vision algorithms in the numerical part of optical mapping has driven recent advancements that allow one to perform optical mapping with moving tissue, see section 1.3. Optical mapping employs fluorophores to measure wavelength-dependent light-tissue interactions across fields of view ranging from hundreds of micrometers to several centimeters. The fluorophores are typically fluorescent dyes introduced to the tissue via perfusion. However, fluorophores can also be readily existent and native to genetically modified tissues. Tissues are illuminated using wavelength-selected excitation light. The light excites the fluorophores, which alter their fluorescing properties in response to physiological activity. These effects are then simultaneously mapped across the tissue as it is collected by an optical system comprising optical filters, lenses and a detector. A dichroic mirror separates the excitation and the fluorescent light and an emission filter selects parts of the emission spectrum and lets them pass onto the detector. The detector measuring the emission light is typically the sensor of a high-speed, high dynamic range, camera operating at speeds ranging typically in between 100 to 10,000 frames per second. The high dynamic range of the camera is prerequisite for the ability to amplify the usually small-amplitude fluorescent signals ΔF, which need to be extracted from the overall raw fluorescent light F. While the first optical mapping systems used photodiode arrays (PDA) as detectors, modern systems are using charge-coupled devices (CCD or EMCCD) or complementary metaloxidesemiconductor (CMOS or sCMOS) sensors. The sizes of the detector arrays typically range from 100×100 to 512×512 pixels in modern cameras, where there is a trade-off between image resolution and maximum frame rate.

Optical mapping is most commonly employed to image electrochemical processes, such as action potential activity or fluctuations of intracellular calcium concentrations on the heart surface. The specific combinations of dyes, excitation light and filtering configurations used for probing the specific electrophysiological parameters determine the nature of the fluorescent signal that is measured on the detector. For instance, the widely used potentiometric fluorescent dye di-4-ANEPPS causes small intensity drops that directly reflect the course of an action potential, see Fig. 1 (the original signal was inverted). During the depolarization of a cardiac myocyte the emission spectrum of the dye is shifted towards shorter wavelengths. Filtering the emission light with a long-pass emission filter with a cut-off frequency positioned within the slope, close to the peak of the emission spectrum results in an emission intensity change on the detector that is approximately linearly proportional to the membrane potential. For di-4-ANEPPS the typical fractional change ΔF of the overall fluorescent light F is in the order of $3 - 10\%$ per 100 mV. As a consequence, one can observe waves of small-amplitude intensity modulations in the emission light on the detector, which represent action potential waves. Fractional changes ΔF can be both smaller and range in the order of a few percent and be just barely above noise, for instance when mapping the response of fluorophores in transgenic tissue, and larger, for instance when using dyes such as Rhod-2AM or FluoVolt, which may produce fractional changes of about 20% per 100 mV respectively. Independently of the particular fractional change, the optical signals are prone to perturbations and their acquisition requires sensitive imaging equipment and stable imaging conditions, particularly if one discusses the technique in the context of motion. The intensity modulations immediately caused by electrophysiological activity can easily be superimposed and distorted or masked by flickering of unstable light-sources, jitter of the exposure times of the detector or other noise. Motion artifacts arise in optical mapping experiments due to the interruption of the highly sensitive measurement as the imaged tissue contracts, deforms or moves, see section 1.2.

Optical mapping can be performed acquiring multiple parameters simultaneously using multi-bandpass filtering and multiple fluorescent dyes together. Simultaneous mapping of membrane potential and intracellular calcium, for instance, has been introduced by Efimov et al. (1994) and Choi and Salama (2000). In the dual optical mapping system reported by Choi and Salama (2000), two synchronized and geometrically aligned detector arrays measure voltage and calcium simultaneously. Dual optical mapping with only a single camera has been proposed by Lee et al. (2011). In this approach, voltage and calcium is measured consecutively by rapid switching of two excitation light sources and an appropriate emission filter configuration. The development of multi-camera systems for panoramic optical mapping was introduced by Kay et al. (2004), Rogers et al. (2007) and Qu et al. (2007). Panoramic optical mapping aims at imaging larger parts or the entire surface of the heart by filming the heart from multiple perspectives simultaneously, reconstructing the three-dimensional surface geometry and projecting the video data onto the static surface. With

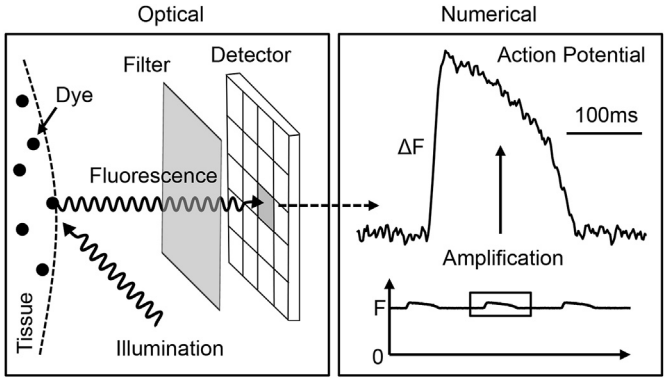

Fig. 1. Optical mapping is a combination of optical and numerical techniques: the optical part consists of fluorescent dyes, illumination, filtering and high-speed detector technology able to resolve small changes in fluorescence caused by physiological activity at a high temporal (*ms*) resolution. The numerical part comprises algorithms for the amplification of the small signals (action potentials) and their visualization as spatio-temporal patterns. The adaptation of computer vision algorithms in the numerical part has driven recent advancements that allow to perform optical mapping with moving tissues.

panoramic optical mapping it has been possible to obtain 360° visualizations of reentrant wave dynamics during ventricular tachycardia and fibrillation on the entire surface of isolated hearts (Rogers et al., 2007). While the recent developments of optical mapping have continuously increased the capabilities of researchers to study the heart's electrophysiological activity, optical mapping is yet not widely performed with contracting hearts. For a general review of optical mapping see Efimov et al. (2004); Salama (2001); Herron et al. (2012).

1.2. Motion artifacts

Optical mapping is very sensitive to any contractile or translational motion. Even the slightest motion may result in a significant distortion of the measurement of action potentials or calcium transients on the heart surface. The distortions that can be observed in the measurement data may range from moderate deflections of the signals, for instance, if hearts exhibit residual contractions after mechanical or pharmacological motion inhibition, to completely obscured signals when imaging freely beating hearts. Generally, the distortions are referred to as *motion artifacts*. Motion artifacts are recognized since the early days of optical mapping (Brandes et al., 1992; Knisley et al., 2000; Lee et al., 2001), since hearts exhibit frequently residual contractions despite motion suppression. While such residual motion artifacts have always provoked efforts to suppress motion as efficiently as possible, nowadays cardiac motion is recognized as valuable information rather than an undesired root for artifacts, that is worth being analyzed during optical mapping (Bourgeois et al., 2011; Christoph, 2015; Zhang et al., 2016; Kay and Efimov, 2016).

Motion artifacts originate, mainly and firstly, from a *dissociation* of the tissue segment aimed to be measured on the heart surface and the corresponding pixel on the detector due to motion of the heart with respect to the detector, see Fig. 2. Motion leads to sliding of the image scene through the detector plane. As a result, fluorescence is measured from various locations instead of from only one. Fig. 2a) shows two video images of a contracting rabbit heart, mapped with voltage-sensitive staining (di-4-ANEPPS) during sinus rhythm. The heart deforms strongly and individual tissue segments exhibit large translational motion. A tissue segment that was tracked throughout the video sequence numerically is indicated by black dots for two different times t_1 and t_2 in the cardiac cycle. The distance between the two dots indicates how far the tissue segment has moved. Furthermore, it becomes immediately apparent that it is impossible to measure the fluorescence emitted by the tissue segment using the same pixel of the detector. The tissue segment and the pixel become dissociated. The schematic drawing illustrates the corresponding situation, in which the allocation of a pixel with a particular tissue segment becomes compromised due to motion. A brighter piece of tissue could move into the position, in which earlier a darker piece of tissue was located and vice versa. The misalignment in the measurement procedure may not always be apparent, in particular, if the tissue surface exhibits a homogeneous texture or vanishing image intensity gradients. In terms of signal deflections, the misalignment becomes critical if the scene in the fluorescence emission image exhibits large differences in intensity baseline. This becomes the case if, for instance, the heart is filmed in front of a dark background, is illuminated inhomogeneously, or if other objects in the experimental setup obstruct the field of view or create shadows on the heart surface. However, even if the scene is illuminated homogeneously and shows only a locally contracting ventricular wall, the tissue surface itself typically exhibits a heterogeneous texture consisting of brighter and darker anatomical structures that can range in their intensity variations easily in the same order as the small, physiology-related fractional changes ΔF in fluorescence intensity, see Fig. 2. Fig. 2b) illustrates how in such cases even small amplitudes of motion can cause significant motion artifacts. The data shows the left ventricular surface of a contracting, fibrillating rabbit heart filmed using voltage-sensitive optical mapping (Christoph, 2015). The local texture reflecting the tissue anatomy is clearly visible as a network-like grayscale pattern. Local shifts due to motion of the tissue are relatively small, but range in the order of a few pixels ($1-3$ pixels). The two optical traces on the right were obtained from two adjacent sites on the surface. Despite their proximity, the time-series that were obtained from the corresponding pixels reveal a significant difference in baseline. The signal strength of the sequence of action potentials itself, indicated by gray bars, is smaller than the difference in baseline. It becomes obvious that in this situation even small shifts of the tissue can lead to strong motion artifacts. The time-series contain a significant drift of the baseline and the normalized videos (not shown) show the typical high-frequency spatial pattern that is characteristic for motion artifacts.

Motion artifacts also originate from *illumination changes* due to relative motion between the heart surface and the light sources as the heart moves, see also Fig. 2. The illumination in optical mapping setups is inhomogeneous. As the heart beats, it changes its position and orientation with respect to one or multiple different light sources. These light sources cause an illumination intensity distribution or light-field in three-dimensional space with local minima and maxima in illumination intensity. As the heart moves through the scene, illumination changes may lead to baseline drifts, which then add to motion artifacts already caused by dissociation. Motion artifacts caused by motion in an inhomogeneous light-field are likely to emerge particularly during sinus rhythm, when overall translational motion of the heart is large, and often much larger than during pacing or arrhythmic cardiac activity. Illumination motion artifacts are likely to occur in video data that shows large intensity gradients, for instance, dark vignettes towards the boundaries of the video image, but they may also occur in video data that shows a seemingly homogeneously illuminated heart. Motion artifacts may also originate from other factors, such as absorption and emission changes of fluorescent dyes during deformations of the tissue, but their contribution is difficult to determine.

Motion artifacts are most easily identifiable by the distortions that they introduce to the characteristic course of the cardiac action potential. Typically, the steep upstroke may become disrupted or the long repolarization plateau of the action potential is shortened or elongated or includes other deflections that cause an action potential shape that can be clearly separated from its normal morphology. In Fig. 2a), the gray time-series illustrates how motion may alter the shape of the action potential. For comparison, the black trace shows the evolution of the action potential recovered after motion tracking and stabilization, see section 1.3. However, the manifestation of motion artifacts can be manifold and does not always have to be immediately apparent. The entire time-series may contain baseline drifts or modulations, that vary with the amplitude and frequency of the motion. Video images, in which the signals were converted by normalizing the individual time-series to their maximal and minimal intensity values in time, typically include a high-frequency spatial pattern that is modulated by the motion occurring in the scene. The strength of motion artifacts increases with the amplitude of the shifts of the tissue and the local intensity gradients present in the video image. With large

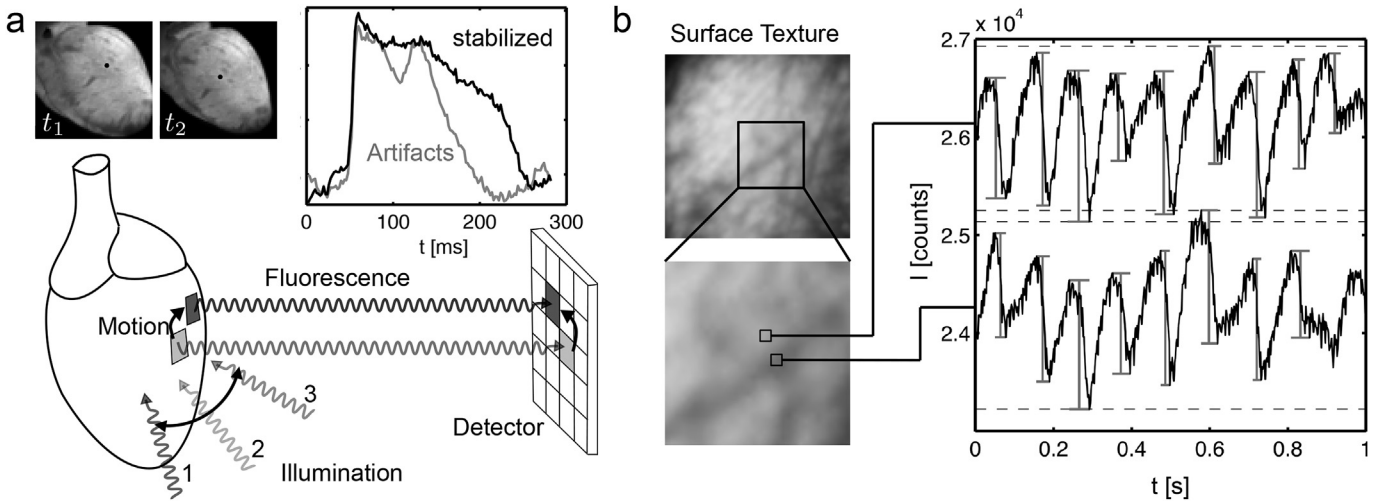

Fig. 2. **a**) Motion artifacts in optical mapping studies caused, firstly, by dissociation of measurement site on heart surface and pixel on detector due to relative motion and, secondly, by illumination changes due to relative motion between heart and light sources (here 1, 2 and 3 with different intensities). Black dots on heart surface in video images indicate same, tracked tissue segment during two different times t_1 and t_2 in the cardiac cycle during sinus rhythm. The corresponding raw optical trace (gray) without motion tracking and compensation contains significant distortions of the action potential. The stabilized optical trace (black) obtained through tracking and co-moving analysis shows significantly reduced motion artifacts. Schematic drawing adapted and modified from Stender et al. (2013). **b**) Optical traces during ventricular fibrillation on left ventricular surface of contracting rabbit heart obtained during voltage-sensitive optical mapping. The traces were measured in two adjacent sites being located only a few pixels ($5 - 10$) apart from each other on the detector. The difference in baseline ($\sim$ 2000 counts) in the time-series can cause potential motion artifacts. The amplitude of the signal (gray bars) in both traces is in the order of $\Delta F \sim 1000$ counts. Even very slight motion can cause the brighter or darker patterns from neighbouring pixels to move into the position from which the time-series was obtained (dissociation). As a consequence, the baseline of the time-series is modulated.

translational motion and large intensity gradients in the video images, motion artifacts can even become so strong that action potentials become entirely obscured or do not remain recognizable any longer at all in both the time-series or the normalized videos.

Motion has been suppressed in optical mapping studies by mechanically restricting hearts (Laurita et al., 1998) or reducing the calcium concentration in the perfusate (Salama and Morad, 1976). However, more commonly, the cardiac contractile activity itself has been suppressed pharmacologically by applying excitation-contraction uncoupling agents such as diacetyl monoxime (DAM), (Li et al., 1985), 2,3-butane-dione monoxime (BDM) (Gwathmey et al. (1991)), or Blebbistatin, (Fedorov et al., 2007). However, the species-dependent electrophysiological side-effects of these agents have to be carefully considered. Riccio et al. (1999) show that diacetyl monoxime reduces the slope of the restitution relation, prevents the induction of ventricular fibrillation and converts existing ventricular fibrillation into a periodic rhythm in dog hearts. Baker et al. (2004) investigated the effects of mechanical uncouplers, diacetyl monoxime, and cytochalasin-D on the electrophysiology of perfused mouse hearts and found that the uncouplers cause a prolongation of action potential durations and refractory periods, which, in principle can have proarrhythmic effects. Fedorov et al. (2007) introduced Blebbistatin as an electromechanical uncoupler. While they did not observe any appreciable electrophysiological side-effects, Brack et al. (2013) report that Blebbistatin may significantly affect cardiac ventricular electrophysiology and the induction of ventricular arrhythmias in rabbit hearts. Swift et al. (2012) describe other methodological issues associated with the use of Blebbistatin, such as blockage of the microcirculation due to precipitate, effects onto tissue metabolism and spectral shifts in endogeneous fluorescence. Lou et al. (2012) found that BDM in contrast to Blebbistatin flattens the action potential duration restitution curve and reduces the action potential wavelength. Furthermore, they found that the incidence of sustained arrhythmias is much lower under Blebbistatin than under BDM and that while arrhythmias under BDM were able to stabilize, the arrhythmias under Blebbistatin were unstable and terminated spontaneously. We frequently find that the heart rate decreases during the administering of Blebbistatin, presumably due to blockage of the heart's microcirculation. The controversial experimental findings and documented issues raise concerns regarding the validity of optical mapping studies, in which uncoupling agents have been used and highlight the need for alternate approaches.

1.3. Motion artifact correction

Motion artifacts caused by dissociation can in principle be overcome by introducing a co-moving video analysis that measures the fluorescence from the heart surface along a trajectory that follows precisely each tissue segment as it moves through the scene. Without motion, the measurements can be performed conveniently *independently* in each pixel, as the allocation of one pixel with an imaged subregion of the tissue remains intact over time. With motion, however, this approach becomes quickly compromised. Coherent undistorted wave patterns can only be retrieved by consecutive measurements in multiple pixels along the tracked trajectories describing the motion of the tissue. The trajectories together need to describe the movement of a continuously deforming medium. Performing such a co-moving video analysis is technically challenging, as small deviations of the tracked trajectories from the real trajectory of single tissue segments can, similarly as slight residual motion in uncoupled hearts, also lead to strong motion artifacts. In other words, it is required to capture the deformations of the cardiac muscle sufficiently accurate using image registration and motion tracking techniques that are able to resolve shifts and non-rigid body motion of the tissue at sub-pixel spatial resolutions.

Recent studies have demonstrated that motion artifacts can be reduced in optical mapping of strongly contracting hearts using computer vision techniques (Bourgeois et al., 2011; Christoph, 2015; Zhang et al., 2016). The studies employed non-rigid image registration and motion tracking techniques to compensate motion artifacts and to simultaneously capture and quantify mechanical deformations of the heart. Image registration uses numerical

measures of image similarity to compute shifts and affine deformation maps in between images. The shifts can be used to deform or morph images such that they match the reference image. This procedure, generally referred to as warping, yields motion-stabilized video sequences, in which motion is suppressed if applied to all images in a video sequence. If the original intensity values in the video frames are preserved, but only the spatial configuration of their pixels changes, the warped image sequence corresponds to the co-moving video sequence, in which motion-compensated artifact-free time-series of action potentials may be retrieved. The original video data needs to be resampled according to the tracked configurations of the tissue. Depending on the image registration algorithm, shifts can be detected for manually selected or automatically identified points, which themselves can be either sparsely, densely, evenly or unevenly distributed throughout the image. Algorithms may produce displacement maps indicating global or local shifts, considering rigid or non-rigid deformations.

Using numerical image registration techniques, tracking of the heart's surface motion has been performed either by tracking markers attached to the tissue surface (Bourgeois et al., 2011; Zhang et al., 2016) or by tracking anatomical landmarks, a unique texture or other characteristic detectable features exhibited by the tissue itself (Rohde et al., 2005; Svrcek et al., 2009; Rodriguez and Nygren, 2012, 2015; Christoph, 2015; Khwaounjoo et al., 2015). The first approach has the advantage that the position of markers can be identified more easily and reliably in that the size, shape and distribution of markers is known. Also, marker pairs showing the same marker in two different video images can be associated possibly more easily with each other as their configuration in which they are attached to the heart surface is known. However, markers restrict the spatial resolution at which the morphological configuration of the tissue is captured. To increase spatial resolution, interpolation of the data may become needed in between markers (Bourgeois et al., 2011; Zhang et al., 2016). It is furthermore possible that the attached markers can cause mechanical stresses as the heart wall deforms. The latter approach that relies on tracking of visible features has the advantage that the heart's wall is unaffected by possible mechanical obstructions and that the spatial resolution at which the morphological configuration can be captured is only limited by the frequency of detectable, separate features on the heart surface that can be resolved and tracked by the image registration algorithm (Christoph, 2015). In principle, tracking can be performed on a pixel or sub-pixel level, such that highly resolved motion-stabilized videos can be obtained (Christoph, 2015). The identification and tracking of complex landmarks, shapes or features may require more sophisticated image registration techniques and could impose other restrictions such as loss of image similarity between images, if the tissue landmarks or features undergo morphological changes during deformations or movements and perspective changes. Rohde et al. (2005) demonstrated firstly that it is possible to retrieve motion-artifact reduced time-series and optical maps of action potential propagation across the surface of contracting rabbit hearts using image registration techniques. However, in their study the image registration method considered only global motion including translational, rotational and shearing motion, suggesting that finer nonlinear local deformations were likely still present in the motion compensated video data. Their data yet contains residual motion artifacts. The relatively good outcome of their motion compensation, however, suggests that the contractions of the hearts were moderate. Svrcek et al. (2009) similarly computed rigid translational and rotational motion, however, in smaller subregions of the video images. Both studies used similar measures of image similarity, correlation indices and image intensity differences, to identify shifts in between images. Rodriguez and Nygren (2012, 2015) identified individual anatomical landmarks distributed sparsely across the heart surface to track and compensate motion and to reduce motion artifacts in time-series. Christoph (2015) and Khwaounjoo et al. (2015) computed non-rigid affine deformation maps describing the continuous motion and deformation of the tissue using block-matching and optical flow algorithms detecting displacements in every pixel, using similar measures of image similarity such as image intensity differences. In particular Christoph (2015) demonstrated that coherent spatio-temporal patterns of action potential wave spread across the strongly deforming and moving heart surface can be recovered, and that the electrical and elasto-mechanical activity that was measured simultaneously, can be related to each other. Another imaging technique for the capturing of heart wall surface mechanics at very high spatial resolutions is structured light imaging (Laughner et al., 2012).

Lastly, motion artifacts caused by, for instance, relative motion between the heart and the illumination can be suppressed using ratiometric imaging (Brandes et al., 1992; Knisley et al., 2000; Hooks et al., 2001; Tai et al., 2004; Svrcek et al., 2010; Bachtel et al., 2011). Ratiometry analyzes signal information that is available at two separate bandwidths in the emission spectra of particular ratiometric fluorescent dyes to identify signal components that have been caused by motion. While ratiometric optical mapping may reduce motion artifacts caused by relative motion between the tissue and the illumination, it may not principally avoid other undesired effects of motion. The technique, unlike image registration, lacks to solve the dissociation problems occurring in the measurement. Nevertheless, ratiometry may be used as a complementary technique in conjunction with image registration and tracking techniques (Bourgeois et al., 2011). In this work, we also report on a novel purely numerical technique for the compensation of motion artifacts caused by relative motion of the illumination.

2. Materials and methods

Contracting isolated Langendorff-perfused rabbit hearts ($N = 2$) were filmed using a panoramic multi-camera optical mapping system consisting of four calibrated high-speed cameras. Hearts were filmed beating freely during sinus rhythm. After imaging the contracting, fluorescing hearts and capturing the action potential wave activity on its deforming surface, the excitation-contraction uncoupling agent Blebbistatin was administered to inhibit contractile motion of hearts. The three-dimensional outer shape of the non-contracting hearts was reconstructed optically using shape-from-silhouette algorithms. The three-dimensional surface geometry was then deformed using displacement data, obtained through marker-free tracking of the heart's surface during optical mapping, i.e. relying only on the heart's intrinsic superficial features. Action potential wave spread was then visualized on the reconstructed three-dimensional deforming ventricular surface geometry using co-moving video analysis. The experimental procedure is displayed in Fig. 3b), see also section 2.2.

2.1. Experimental setup

The experimental setup consisted of a panoramic multi-camera optical mapping system with 4 high-speed EMCCD cameras (Evolve 128, Photometrics Inc., USA, 128 × 128 pixels, 16 bit dynamic range) and a retrograde Langendorff-perfusion system with an eight-sided bath with glass walls, see Fig. 3a). Isolated rabbit hearts were positioned at the center of the equilateral, eight-sided bath (window width = $40mm$, height = $120mm$) and filmed with the 3 or 4 cameras through 3 or 4 adjacent windows respectively, the cameras being positioned similarly far from the heart on rails

separated by angles of 45°. Voltage-sensitive dye was excited using 6 light-emitting diodes operating at wavelengths of 532*nm*. Hearts were filmed using high-aperture lenses (objectives Fujinon 1.4/9*mm*, Fujifilm Corp.) and long-pass filtering (Edmund Optics, transmission >610*nm*) to filter the fluorescent light emitted from the heart surface. The high-speed cameras were synchronized via TTL triggering and recordings were obtained at a frame rate of 500*Hz*. An additional high-resolution color DSLR camera (Canon EOS 500D, EF-S 18–55 mm lens) was positioned looking through the back right window (see Fig. 3c) and used for taking high-resolution photographs of the heart during the geometry reconstruction at the end of the experiment. Hearts were retrogradely perfused using a Langendorff-perfusion system (Hugo-Sachs Apparatus, March-Hugstetten, Germany). The system comprised a motorized rotary stage (T-RSW60A, Zaber Technologies Inc., Canada) providing the possibility to rotate the heart automatically and at high angular precision for full 360° rotations around the vertical axis. Custom-written software allowed controlling motor rotation and synchronized triggering of the high-speed cameras and the high-resolution DSLR camera.

2.2. Experimental protocol

Experiments were conducted in 4 consecutive parts, see Fig. 3b). In the first part of the experiment, cameras were aligned and calibrated, see section 2.4. In the second part of the experiment, fully contracting hearts were filmed using voltage-sensitive staining, mapping the electromechanical activity of the heart. Throughout this part, pharmacological excitation-contraction uncoupling agents were not used and hearts were allowed to contract freely. Hearts were stained using voltage-sensitive dye di-4-ANEPPS (1 ml, 1 mM, bolus injection into bubble trap, recirculated). To guarantee homogeneous distribution of the dye in the tissue, filming was started at the earliest 5 min after the dye was administered. Normal sinus rhythm was then filmed within approximately 5 min. In the third part of the experiment, Blebbistatin (−) (8–9 ml, 10 mM, pre-diluted in 0.8 L Tyrode, pre-heated at 37.0±0.5°C, perfused and then recirculated with other Tyrode, see below) was administered approximately 5 min after the start of the second part of the experiment and after having acquired sufficient recording data. Typically, all visible contractile motion had disappeared approximately 10 min after the administration of Blebbistatin. In the fourth part of the experiment, the outer three-dimensional shape of the non-contracting, quiet heart was captured optically, see section 2.6. Electrocardiograms were recorded using two thin electrodes inserted into the bath and acquired using a data acquisition system (MP150, Biopac Systems Inc., Goleta, USA) acquiring data at a sampling rate of 2.0 kHz throughout the entire duration of the experiment.

2.3. Preparation of isolated hearts

New Zealand white rabbits (2.5–3.5 kg) were heparinized and anaesthesized using 4.0 ml Trapanal (single intraveneous injection, Thiopental-sodium solution, 50 mg/kg) diluted in 10.0 ml isotonic sodium chloride (NaCl). Hearts were excised rapidly and inserted into cardioplegic solution for temporary cessation of cardiac activity. Tyrode (15 l) solution was prepared. Isolated hearts were transferred quickly into a bath filled with warm, oxygenated (95% O2, 5% CO2) Tyrode and connected to a retrograde Langendorff-perfusion system (Hugo-Sachs Apparatus, March-Hugstetten, Germany). The flow rate of the perfusate was 30 ml/min at a perfusion pressure of 50±5 mmHg. Tyrode was kept at a constant temperature of 37.0±0.5 °C (custom-made temperature control, Max Planck Institute for Dynamics and Self-Organization, Göttingen, Germany) and was constantly reperfused. Blebbistatin was administered 5 min after the start of the imaging experiment. Uncoupling agents were not applied during the initial phase or first

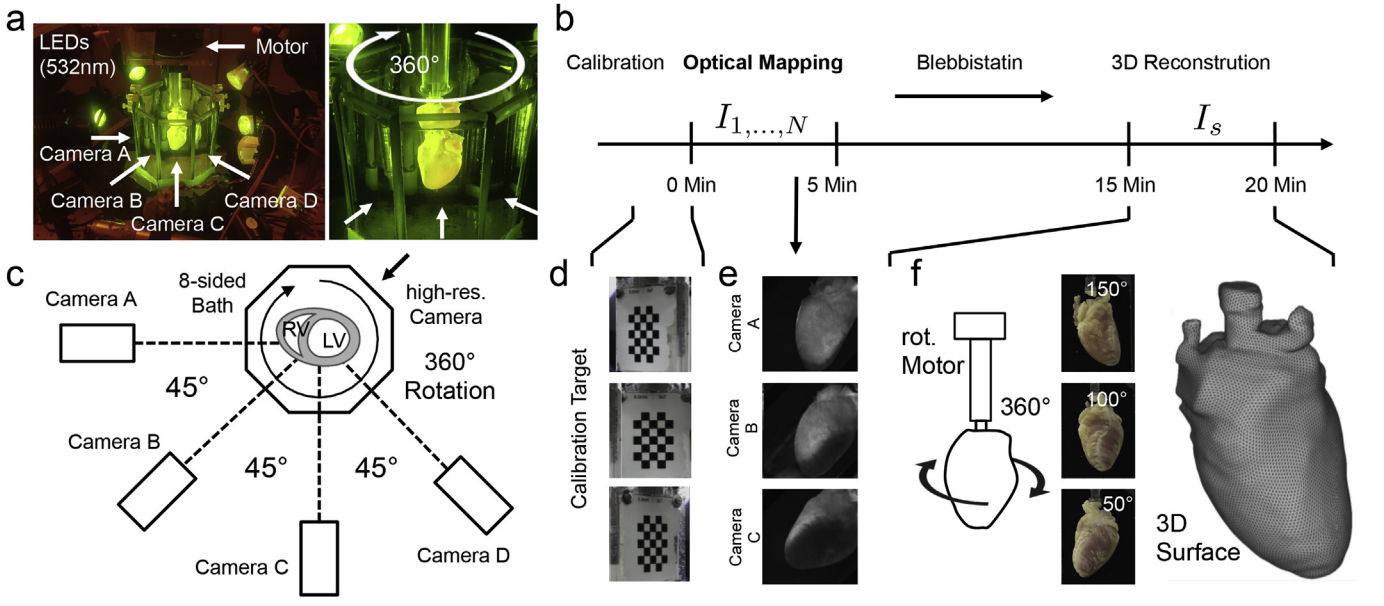

Fig. 3. Experimental setup for panoramic electromechanical optical mapping of contracting isolated Langendorff-perfused rabbit hearts. Multi-camera setup using up to 4 calibrated high-speed cameras (128 × 128 pixels, 500*Hz*) and additional high-resolution DSLR camera and rotational stepping motor for calibrating the cameras. **a**) Bath, illumination and perfusion system with motorized rotational attachment of heart hanging in center of bath. Heart filmed through 4 adjacent windows. **b**) Experimental protocol: calibration prior to the imaging experiment, followed by electromechanical optical mapping experiment with contracting heart (0 – 5 minutes), administering of Blebbistatin (5 – 10 minutes) and optical reconstruction of non-moving three-dimensional surface of hearts (15 – 20 minutes). **c**) Alignment of cameras around bath. Cameras A, B, C and D oriented at 45° angles filming heart through 4 adjacent windows, all cameras filming ventricular heart wall including parts of the right and left ventricle. **d)** Calibration target at different rotational angles. **e)** Optical mapping video images from the three different high-speed cameras A, B, C. **f)** Rotating of heart for surface reconstruction, high-resolution photographs showing imaged part of heart for three different angles and reconstructed three-dimensional geometry mesh.

5 min of the imaging experiment. Any mechanical pressure to the hearts was avoided to prevent compression of the coronary arteries. All procedures regarding care and use of animals were in accordance with German animal welfare law.

2.4. Camera calibration

All cameras were calibrated before the start of the imaging experiment. A flat, rectangular calibration target with checkerboard pattern (5×7 square tiles, 5 mm lattice constant) was attached to the motor and placed inside the filled bath. The motor rotates the calibration pattern around the vertical Z-axis, in order to ensure that for each camera multiple photos of the pattern facing the camera can be taken at defined angular positions. The mounting of each camera was carefully adjusted, such that the calibration pattern remained fully visible inside the field of view for all rotational positions, and the imaging plane was oriented parallel to the glass window, which is important to avoid strong distortions due to diffraction. The focus of the lenses was adjusted to ensure sharp imaging of the calibration pattern and the heart surface. With the combination of lenses and the high power illumination, it was possible to perform imaging with sufficiently closed apertures to produce large focal depths. As a result, the heart surface was in focus whenever the calibration patterns were in focus and also remained in focus as the heart moved back and forth. We did not observe defocusing of the heart surface. From here on, all parameters which affected the imaging had to be held fixed, i.e. the cameras' position and rotation as well as the lens focus were not changed during the subsequent experiment. The calibration target was rotated for a full 360° rotation in 72 steps of 5°, and a video image or high-resolution photograph was taken with the cameras (Evolve high-speed cameras and high-resolution DSLR camera) for each step respectively. For this step a custom-written software was used. The software controls the stepper motor of the rotary stage and sends trigger signals to the programs controlling the cameras.

After the experiment, the imaging properties of each camera were calibrated using the open source computer vision library OpenCV 3.1.0 (Itseez/Intel, USA, 2015), which provides methods for camera calibration with a pinhole camera model. The model's central equation projects a point (X, Y, Z) from three-dimensional world coordinates to two-dimensional image coordinates (x, y):

$$s\begin{pmatrix} x \\ y \\ 1 \end{pmatrix} = \begin{pmatrix} X' \\ Y' \\ Z' \end{pmatrix} = \begin{pmatrix} f_x & 0 & c_x \\ 0 & f_y & c_y \\ 0 & 0 & 1 \end{pmatrix} \left[\begin{pmatrix} r_{11} & r_{12} & r_{13} \\ r_{21} & r_{22} & r_{23} \\ r_{31} & r_{32} & r_{33} \end{pmatrix} \begin{pmatrix} X \\ Y \\ Z \end{pmatrix} + \begin{pmatrix} t_1 \\ t_2 \\ t_3 \end{pmatrix} \right] \tag{1}$$

Here, rotation matrix $r_{i,j}$ and translation vector t_i position the camera relative to the world origin and are called *extrinsic* parameters. x and y are horizontal and vertical image coordinates of the projected point in pixel units with the origin in the upper left corner of the images. The point (c_x, c_y) is the principal point of the optical axis, which usually is located near the image center. f_x and f_y are the focal lengths expressed in pixel units. Parameter $s = Z'$ performs the perspective division.

Equation (1) describes the projection for an ideal lens, which is free of distortions (therefore the term *pinhole* model). The model is extended with nonlinear equations, in order to account for real lenses with radial and tangential distortion (for details, see OpenCV documentation (Itseez/Intel, USA, 2015)). The lens-specific focal lengths, principal point, and distortion coefficients are called *intrinsic* parameters.

All model parameters were estimated for each camera with the following steps, using methods provided by OpenCV library: First, the pixel locations of the corners of the checkerboard images were determined to sub-pixel accuracy. Based on this the intrinsic parameters of the model were estimated, including distortion parameters. Then the images were undistorted, such that all subsequent computations could be performed using equation (1). The three-dimensional locations of the checkerboard corners were computed for each of the 72 rotated positions, with respect to a global coordinate frame located at the center of the calibration target. Finally, the position and orientation (extrinsic model parameters) were estimated for each camera with a Levenberg-Marquardt optimization algorithm, given the intrinsic parameters and corresponding sets of 3D positions and 2D pixel locations of the checkerboard for the respective camera.

2.5. 2D motion tracking

Motion tracking was performed to obtain two-dimensional in-plane displacement vector field data indicating the shifts of the tissue seen in each of the 3 or 4 recordings obtained from the 3 or 4 cameras. Markers attached to the surface of the heart to facilitate or assist motion tracking were not used. Short video sequences of $1000 - 5000$ frames of the optical mapping recordings showing the beating heart for at least $4 - 5$ cycles were extracted and converted into video sequences featuring the local tissue contrast. Each pixel's intensity value $I(x, y, t)$ was renormalized by the maximal and minimal intensity values within a small disk-shaped sub-region $\mathcal{S}_{(x,y)}$ around the pixel:

$$C(x, y, t) = (I(x, y, t) - \min(\mathcal{S}))/(\max(\mathcal{S}) - \min(\mathcal{S})) \tag{2}$$

the sub-region $\mathcal{S}_{(x,y)}$ typically retaining a diameter of 5–7 pixels. The conversion produced video sequences, in which the local tissue contrast is maximally intensified and the tissues' features and its unique local texture become very pronounced, see Fig. 4. At the same time, larger-scale intensity gradients across the images were removed. Motion was then tracked in the resulting contrast-enhanced videos. The typical frequency of the detectable features in the video images is a few pixels (3–10) and given by the granular appearance of the tissue after staining, see also Fig. 2b). Two-dimensional in-plane displacements $\mathbf{u}^k(x, y, t) \in \mathbb{R}^2$ were determined for each pixel (x, y) in every frame $C_c^k(x, y, t)$ $(t \in [1, \ldots, N])$ throughout the contrast-enhanced video image sequences obtained from each camera A, B, C and D respectively $(k \in [A, B, C, D])$. Local displacements or optical flow in the images were computed using Lucas-Kanade image registration algorithms (Periaswamy et al., 2000).

Depending on the video image quality, two different tracking schemes were applied when registering motion in the video data, see Fig. 5a) and b). The scheme shown in Fig. 5a) was used when it was possible to obtain a complete set of displacement vectors throughout the entire sequence of video images that describe the

shifts of the tissue throughout the images with respect to one video image C_s showing the static, non-moving, uncoupled heart after the application of Blebbistatin. Each frame in the video image sequence was registered individually with respect to the one static video frame showing the possibly deformed but uncoupled heart. The scheme could only be applied if the heart's visual appearance had stayed approximately the same after the application of Blebbistatin. The data shown in Fig. 7 was obtained using this tracking scheme. The scheme shown in Fig. 5b) was used when it was not possible to reliably track all the shifts, because the tissue's appearance had changed significantly in the meantime in which Blebbistatin was applied. In some cases we observed that the image registration algorithm was not able to compute shifts in between certain tissue regions or in all the video images due to lacking image similarity. Over time, the visual appearance of the heart changed presumably due to dye bleaching or wash-out or because the heart deformed significantly and rotated such that parts turned away from the field of view of the camera. Nevertheless, with the two-stage tracking scheme shown in Fig. 5b) we could circumvent these issues and obtain complete tracking data. In a first in-sequence displacement registration step, shifts $\mathbf{u}_t^k(x,y,t)$ of the tissue were derived with respect to one reference frame $C_t^k(x,y,t)$ selected within the video image sequence showing the beating heart shortly before ($25ms \pm 5ms$) the depolarization and contraction of the atria and ventricles during sinus rhythm. Each frame $C_1, \ldots, C_N$ was registered individually with respect to the in-sequence reference frame C_r. Using this displacement data, the video image frames were morphed and resampled to create warped video frames $\tilde{C}^k$, the frames showing a similarly deformed tissue configuration as shown in the reference frame C_r^k. The warped video image sequence was then registered in a second out-of-sequence displacement registration step, in which all warped frames were registered with respect to the video frame C_s^k showing the quiet static heart at the end of the experiment during the reconstruction of the three-dimensional outer heart shape. Then all registerered displacement fields $\tilde{\mathbf{u}}_{r,1}^k, \ldots, \tilde{\mathbf{u}}_{r,N}^k$ from the warped sequence were used to compute an average displacement field $\overline{\mathbf{u}}_{s,r}^k = \frac{1}{N}\sum_{i=1}^{N} \tilde{\mathbf{u}}_{s,i}^k$, which describes the translation and deformation of the heart from the out-of-sequence reference frame C_s^k showing the heart during the static reconstruction part of the experiment to the in-sequence reference frame C_t^k of the first imaging part of the experiment. The averaged displacement field was added to each in-sequence displacement field to obtain a direct deformation mapping $\mathbf{u}_t^k = \mathbf{u}_{s,r}^k + \mathbf{u}_{r,t}^k \approx \overline{\mathbf{u}}_{s,r}^k + \mathbf{u}_{r,t}^k$ from the static out-of-sequence reference frame to each frame showing the

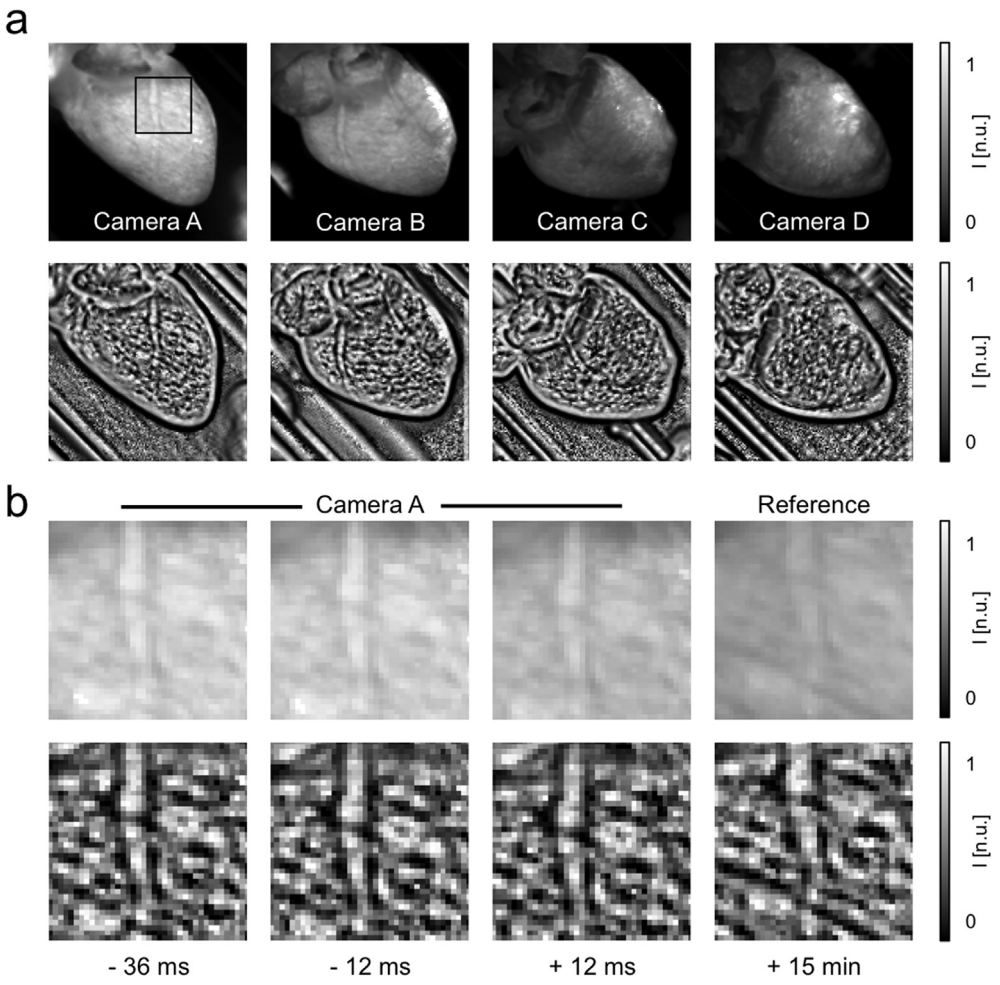

Fig. 4. Motion tracking using contrast-enhanced video images: **a**) Different views of rabbit heart from cameras A, B, C and D during experiment. Top: Pixel intensities normalized to minimal and maximal values in entire video. Bottom: Contrast-enhanced video images used for motion tracking with pixel intensities normalized by minimal and maximal value in local neighbourhood (disk-shaped region $\mathcal{S}$). Local tissue texture free of larger image gradients. **b**) Close-up (black box, camera A) of normal (top) and contrast-enhanced (bottom) video images over time prior to ($-36ms$, $-12ms$) and after ($+12ms$) the depolarization of the ventricles (at $0ms$) and after administering of Blebbistatin ($+15min$). The normal video images at $+12ms$ and $+15min$ are slightly darker due to the depolarization and the decay in fluorescence respectively. The contrast-enhanced video images appear to be unaffected and show very similarly the same anatomical structures. All video images displayed in normalized units [n.u.] on interval [0 1].

beating heart. In a reference frame C_r the tissue is shown in its mechanical reference configuration χ_r, see also Fig. 12. With this tracking scheme, we obtained similar data as shown in Figs. 7 and 8 even in situations when the heart changed significantly in its visual appearance during administering of Blebbistatin. Motion tracking (Matlab), warping and resampling (custom C++ code) and other processing requires approximately 1–3 min of computation time per video image on a single CPU.

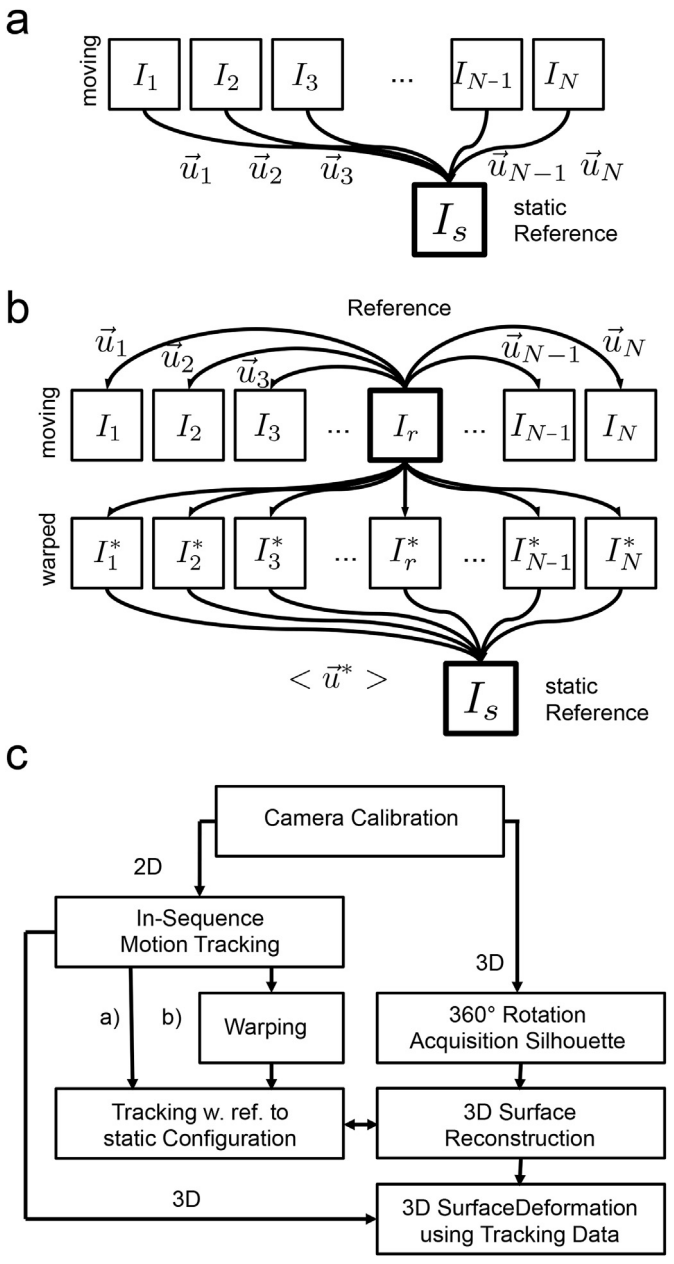

Fig. 5. Motion tracking scheme and deforming surface reconstruction: **a**) Motion was tracked within the image sequence showing the contracting heart with respect to one reference frame I_r selected manually from the sequence, showing the heart shortly before contraction. All other frames $I_1, \ldots, I_N$ were warped to show the heart in the same morphological configuration as in the reference frame. All warped images were registered with respect to the static reference frame showing the uncoupled non-beating heart, to obtain a uniform mapping of the deformation of the heart from the reference configuration to the static, non-moving configuration of the heart. **b**) Schematic diagram of processing steps and their interdependencies: successful reconstruction of the deformations of the contracting heart wall relied on calibrated imaging data, 3D geometry reconstruction and deriving the deformations of the contracting heart with respect to the morphological configuration of the uncoupled heart.

2.6. Heart shape reconstruction and camera images projection

The three-dimensional outer shape of the uncoupled heart was reconstructed approximately 15 min after the start of the experiment and approximately 10 min after administering of Blebbistatin, after all visible contractile motion and swinging or translational motion of the heart had disappeared, see also Fig. 3b) and d). The heart was rotated in 72 steps of 5° and single video images and high-resolution photographs were taken with all cameras in the same way as described in section 2.4. After each 5° rotation step, a delay of 2 – 3 seconds was necessary before the next photo could be acquired, to ensure that residual swinging motion of the heart had sufficiently decayed. The total time required for one full 360° rotation of the heart with acquiring all images at all 72 angles was approximately 5 min. Two rounds of 72 images were taken. First, the EMCCD cameras acquired the fluorescence images of the heart under green LED illumination. Second, the DSLR camera photographed the heart under white light illumination in front of a black background.

After the experiment, the heart shape was reconstructed numerically from the high-resolution color images of the calibrated DSLR camera using shape-from-contour algorithms, as follows: At first, the 72 high-resolution color images were undistorted according to the distortion parameters of the camera model (see section 2.4, equation (1) and its extension). Then, the images were segmented into foreground and background, resulting in black-and-white silhouette images. Based on the 72 pairs of silhouette images and corresponding calibration parameters of the DSLR camera, a point cloud of the heart surface was calculated with the method of Niem (1994), using virtual 'pillars' in x-, y-, and z-direction with a spacing of 0.25 mm, which are truncated by projections of the silhouette masks, resulting in a dense point cloud of the heart's surface. The *Screened Poisson Surface Reconstruction* algorithm (Kazhdan and Hoppe, 2013) was applied to build a triangulated mesh out of the point cloud using the software MeshLab (Cignoni et al., 2008). The triangular mesh was cleaned and uniformly resampled, also in MeshLab, using the *Isoparameterization* algorithm of Pietroni et al. (2010), resulting in a two-manifold, triangular mesh of topological genus 0, composed of approximately 25,000 faces with 0.16 mm^2 mean surface area.

The triangular mesh was further processed to facilitate *texture mapping*. This term from computer graphics describes the method of rendering almost photo-realistic images of objects using polygonal meshes and two-dimensional texture images (maps). First, a spherical parameterization of the convoluted heart surface was obtained using the *FLASH* algorithm (Choi et al., 2015), i.e. a unique three-dimensional point on the unit sphere was assigned to each vertex. Second, two-dimensional texture coordinates were computed for each vertex of the mesh, with a polar azimuthal equidistant projection of the unit sphere to a flat circular map. The center point of the map was aligned with the apex of the heart, and the outer circular border of the map corresponded to the "north" pole located at the aorta. This choice guarantees that the whole ventricular and atrial epicardial surface is mapped to a single connected region inside of the map, which is free of seams, therefore allowing easy application of traditional image and video analysis algorithms.

Images from multiple cameras (or multiple images of the same camera showing the heart under different rotations) were projected onto the mesh and composed into the polar texture map as follows. For each mesh triangle, it was first determined if it was visible in a particular camera view, i.e. inside the field of view and not obstructed. If it was visible, then the three corner points were projected to camera image coordinates according to equation (1).

The enclosed pixels of the camera image were transferred to the corresponding triangular region in the texture map, defined by the texture coordinates of the vertices. This transfer was done using bi-linear resampling and was implemented in OpenGL in order to exploit the capabilities of modern graphics processing units. Texture images obtained from a single camera image with this method, were combined and blended with texture images obtained from other cameras. The blending was done by assigning weights to each mesh vertex for each camera view. The weight was computed from the cosine of the angle between cameras optical axis and the surface normal at the mesh vertex. The cosine was then raised to the power of two, resulting in weights favoring that parts of the surface, where the camera looks onto at a right angle, and diminishing those surface parts, which the camera sees under a flat angle. While the spatial resolution of mesh should be chosen high enough to properly resolve the curvature of the heart surface, the spatial resolution of the texture map can be chosen independently and according to the resolution of the cameras, making it is possible to have a high resolution texture map on a triangular mesh with lower resolution. Figs. 10c) and 11d) show such texture maps composed of 72 color images of the high-resolution DSLR camera. These texture maps were computed at a resolution of 1024×1024 pixels. Texture maps obtained from the low-resolution EMCCD cameras (e.g. Fig. 11e), were computed at a resolution of 512×512 pixels. Since these cameras have a native resolution of only 128×128 pixels, the texture maps were over-sampled in order to prevent loss of information. The process of texture mapping is accurate not only for visualization, but also for calculations, because we use 32bit floating point precision for texture maps of fluorescence in order to ensure that no precision of the camera data (16bit integer) is lost.

2.7. Reconstruction of deforming ventricular surface

The three-dimensional deforming ventricular surface of the contracting heart was reconstructed employing the two-dimensional motion tracking data, see section 2.5, and deforming the three-dimensional reconstructed geometry mesh, see section 2.6, of the non-moving, uncoupled heart. Deforming the mesh is achieved by selecting a vertex of the static reference mesh, projecting its position to 2 or more camera views (if visible), applying the two-dimensional displacements obtained through tracking at those locations and computing the rays of the back-projections to the three-dimensional coordinate system. Computing the intersection points of the rays yields then the new shifted three-dimensional position of the vertex, compare Fig. 6.

In more detail, deforming the mesh is achieved by selecting a vertex m of the static reference mesh, $\mathbf{X}^s_m \in \mathbb{R}^3$, and computing its projection to all (3 or 4) camera views, according to the projection function $\mathbf{pr}_k : \mathbb{R}^3 \to \mathbb{R}^2$, that projects a three-dimensional vector from world coordinates to two-dimensional image coordinates as defined by equation (1), using the calibration coefficients for each camera $k \in [A, B, C, (D)]$:

$$\mathbf{p}^s_{k,m} = \mathbf{pr}_k(\mathbf{X}^s_m) \tag{3}$$

Evaluating the two-dimensional displacement field $\mathbf{u}^t_k : \mathbb{R}^2 \to \mathbb{R}^2$ obtained through tracking at those locations yields the position of the displaced vertex $\mathbf{v}^t_{k,m} = \mathbf{p}^s_{k,m} + \mathbf{u}^t_k(\mathbf{p}^s_{k,m})$ in two-dimensional image coordinates. Theoretically, computing the intersection of back-projected rays would give the three-dimensional position of the vertex of the deformed mesh. However, the three-dimensional displacement of a mesh vertex could not be computed directly from the two-dimensional displacement vectors in the camera images, because the back-projected rays would not necessarily intersect in three-dimensional space. Therefore, we used the *Nelder-Mead* optimization method (or downhill-simplex method) to automatically vary the three-dimensional position $\mathbf{X}^t_m \in \mathbb{R}^3$ of each mesh vertex m at time t, until a best matching position was reached. The optimal position is defined by the global minimum of an objective function $f(\mathbf{X}^t_m)$. The objective function computes the weighted sum over the quadratic differences between the projection of the vertex $\mathbf{p}^t_{k,m} = \mathbf{pr}_k(\mathbf{X}^t_m)$ and the target location resulting from the displacement vector field for each camera view k:

$$f(\mathbf{X}^t_m) = \sum_k w_{k,m} \cdot \|\mathbf{p}^t_{k,m} - \mathbf{v}^t_{k,m}\| \tag{4}$$

The weight $w_{k,m}$ is computed from the angle between the surface normal $\mathbf{n}_m$ at vertex m and the optical axis $\mathbf{z}_c$ of camera k:

$$w_{k,m} = \begin{cases} \cos\varphi & \text{if } \varphi < \widehat{\varphi} \\ 0 & \text{otherwise,} \end{cases} \tag{5}$$

with $\varphi = \angle(\mathbf{n}_m, \mathbf{z}_k)$ and $\widehat{\varphi} = 80°$.

The purpose of the weight is twofold: Firstly, to ensure that those summands are neglected where the surface normal at the vertex points away from the camera, i.e. the vertex is hidden from that camera's view. Secondly, to favor the contributions of those cameras, where the camera looks at right angle onto the surface. The cut-off angle $\widehat{\varphi}$ was introduced in order to completely suppress contributions near the edge of the heart, where the displacement vector field cannot be computed reliably due to interference with the static background. The value of $\widehat{\varphi}$ has to be chosen according to the specific properties of the 2D tracking method. The weights have to be non-zero for at least two cameras, otherwise the deformation cannot be computed and the vertex is discarded.

The result of this reconstruction method is a deforming three-dimensional triangular mesh, which closely follows the real three-dimensional deformation of the cardiac surface for each time step. Therefore the raw fluorescence videos obtained with the 3 or 4 high-speed cameras can be projected onto the deforming mesh and combined into a video texture map of the electrical activity on the epicardial surface, using the exact same method as it is explained in the previous section 2.6 for the static reference mesh.

2.8. Light field estimation for correcting artifacts caused by motion of tissue in inhomogeneous illumination

The three-dimensional motion tracking and stabilization technique described in the previous sections is able to inhibit dissociation motion artifacts, which arise due to the relative motion between tissue and the camera detector, see also section 1.2. However, motion artifacts caused by relative motion between the heart and the illumination or the motion of the heart surface through an inhomogeneous illumination, see also section 1.2, can not be compensated by performing a co-moving analysis. To correct motion artifacts caused by illumination changes, we estimated the strength and variation of the illumination in three-dimensional space surrounding each vertex of the surface mesh and corrected the co-moving measurements of the tissue surface intensity accordingly. With the availability of accurate tree-dimensional tracking data of the contracting surface of the heart, we obtained the possibility to estimate the inhomogeneous three-dimensional light-field using data from the reconstructed trajectories of each vertex and the according intensities measured optically along the trajectories. Fig. 9a) shows the trajectory of a tissue vertex as it moves through space as part of the reconstructed heart surface mesh during the full cardiac cycle and during diastole. The trajectory during diastole indicates intensity fluctuations, which at this stage of the post-processing of the data neither reflect intensity

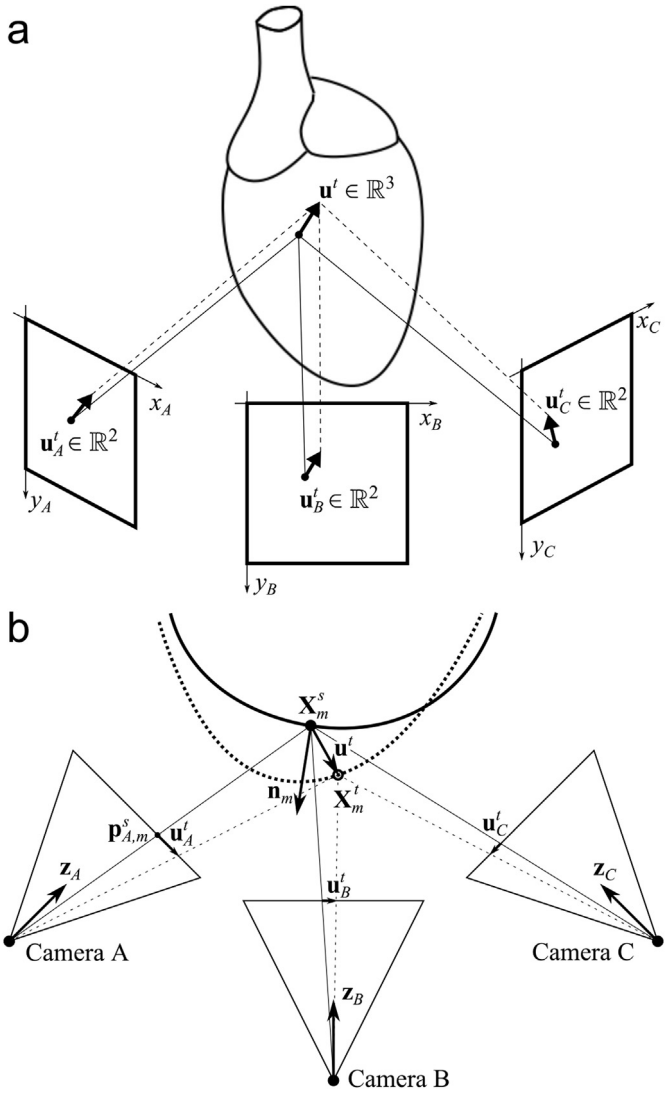

Fig. 6. Schematic drawing of reconstruction procedure of three-dimensional deformation from two-dimensional displacement data of multiple camera perspectives. **a**) Projection of a 3D point on the heart surface into 2D image coordinates for the three cameras. Back-projection of derived displacement into 3D and shift of mesh vertex towards new 3D position. **b**) Top view (not to scale). Outline of the static reference mesh shown as solid curve. Dashed curve shows the reconstructed outline at time *t*.

modulations caused by dissociation or optical flow nor by the action potential, but occur due to motion of the tissue in an inhomogeneous illumination field. We assumed that this inhomogeneous illumination field could be estimated locally around each vertex from the intensity changes appearing at each vertex as it moves during diastole.

The reconstructed trajectory of vertex i as it moves through three-dimensional space is given by $\mathbf{X}_i(t) = (X_i(t), Y_i(t), Z_i(t))$. During this movement the intensity of fluorescence $I_i(t)$ of this particular point on the heart's surface is measured by the high-speed cameras and projected into the video texture. The spatio-temporally varying, measured intensity can be broken down into the following three main components:

$$I_i(t) = l_i(X,Y,Z,t) \cdot f_i(t) \cdot V_i(t) \tag{6}$$

The first factor $l_i(X,Y,Z,t)$, denotes the strength of illumination received by the surface element at vertex i, as it moves through space and time. The second factor, the strength of fluorescence $f_i(t)$ depends on the amount of dye at the surface location of vertex i. The third factor $V_i(t)$ contains the time-variance of fluorescence, which is proportional to the membrane potential.

The spatial and temporal variations of all three factors are a priori unknown, but under further inspection of equation (6), we can identify some helpful simplifications. Firstly, we assume that the net strength of illumination by the various light sources can be approximated by a scalar-valued light field $L(X,Y,Z)$:

$$l_i(X,Y,Z,t) \approx L(\mathbf{X}_i(t)) \tag{7}$$

Secondly, $f_i(t)$ is slowly changing, and can therefore be assumed to be constant throughout the measurement:

$$f_i(t) \approx f_i \tag{8}$$

Lastly, we know that for sinus rhythm, the membrane potential is at resting potential during the diastolic interval (DI):

$$V_i(t) \approx V_i^{\text{rest}} \qquad \text{for } t \in \text{DI} \tag{9}$$

Inserting all these assumptions to equation (6) and reordering leads to:

$$L(\mathbf{X}_i(t)) \approx \frac{I_i(t)}{f_i \cdot V_i^{\text{rest}}} \qquad \text{for } t \in \text{DI} \tag{10}$$

The value of the product in the denominator of the right-hand side is proportional to the resting (or mean) fluorescence intensity at the surface location of the vertex i, and can therefore be taken from the vertex's texture coordinate in the texture image, that is created from the high-speed fluorescence cameras during reconstruction of the heart surface, see Fig. 11e). By inserting all the measured intensities along the trajectories of all vertices during diastole into the right-hand side of equation (10), the left-hand side gives us an approximation of the light field at the corresponding points in three-dimensional space.

It is hard to find a mathematical model for $L(X,Y,Z)$ that globally fits (10) for all the data points of all vertices $i = 1, \ldots, N$. Therefore we chose to estimate the light field locally around the trajectory of vertex i, using all trajectory data during diastole from neighbouring vertices j, lying within a small sphere with radius $r = 2$ mm around the vertex i. We tried to fit the sparse point data to a three-dimensional polynomial P_n up to third order ($n = 3$):

$$P_n(X,Y,Z) = \sum_{m=0}^{n} \alpha_m X^a Y^b Z^c \qquad a+b+c \le m \tag{11}$$

$$P_n(\mathbf{X}_j(t)) \stackrel{!}{=} \frac{I_j(t)}{f_j \cdot V_j^{\text{rest}}} \qquad t \in \text{DI} \tag{12}$$

For our data, we found that a linear ($n = 1$) polynomial approximation of the light-field gave satisfactory results. The polynomial can then be evaluated along the full trajectories throughout the entire duration of the recordings, in particular, for multiple complete cardiac cycles:

$$L_i(t) := P_n(\mathbf{X}_i(t)) \qquad \text{for all } t \tag{13}$$

Finally the time-series of the measured intensities can be corrected:

$$I_i^{\text{corr.}}(t) = \frac{I_i(t)}{L_i(t)} \tag{14}$$

Here, we assumed that it would be sufficient to derive a scalar-

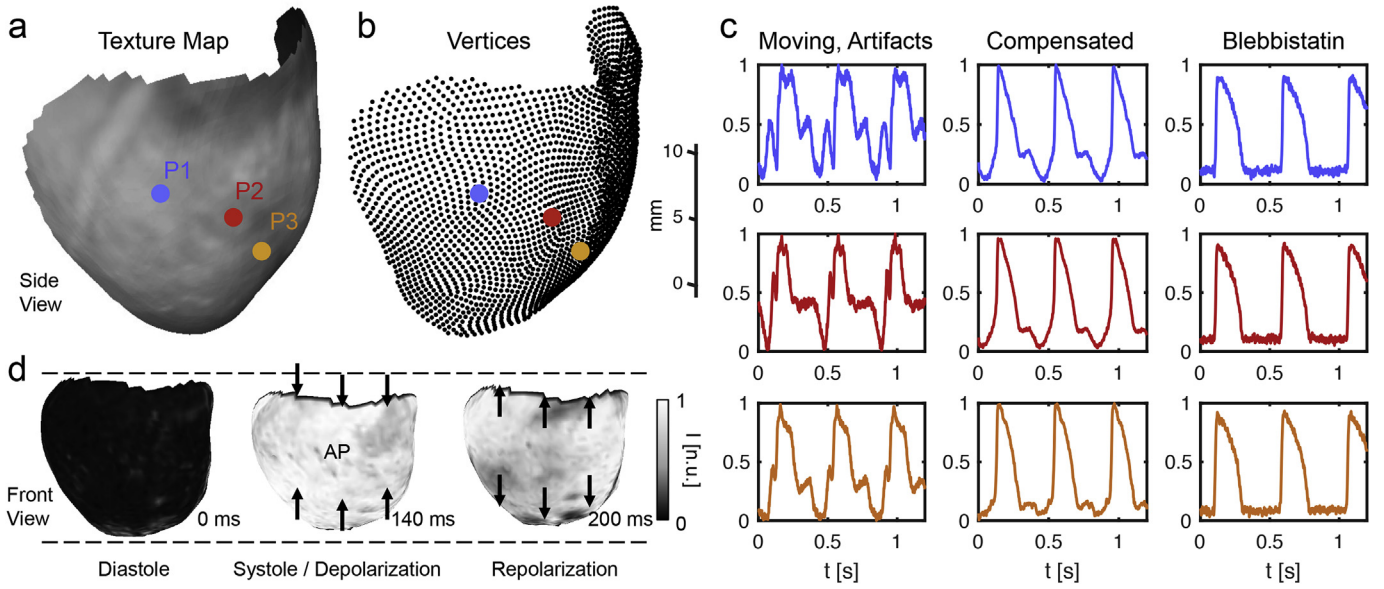

Fig. 7. Panoramic electromechanical optical mapping with beating, strongly deforming hearts. **a)** Reconstructed ventricular surface geometry of beating rabbit heart. Video texture map obtained from 4 cameras (oriented at 45°) projected onto deforming triangular mesh geometry. Mesh consists of 4,405 faces and 2,286 vertices and shows almost 180° of the circumference of the heart and the ventricular wall from apex to base. **b)** Vertex mesh of reconstructed ventricular surface geometry of beating rabbit heart. Trajectories T_i of each vertex i describe motion of tissue surface, see Fig. 8 **c)** Optical traces obtained from 3 sites (P1, P2, P3, red, orange and blue dots) on moving heart surface. Left column: raw traces obtained from single pixels of cameras including heavy motion artifacts resulting from translational motion and deformation of the tissue. Center column: traces after motion tracking, stabilization and light-field correction. Action potential shapes and upstrokes recovered. Visible deflections in diastolic interval. Right column: traces from surface of non-moving, electromechanically uncoupled heart (Blebbistatin) showing action potentials without motion artifacts about 15 min later. **d)** Action potential wave spread across strongly moving and deforming heart surface during sinus rhythm (see also Supplementary Movie 2). Maps were computed from the time-series data shown in the central column in panel c). Maps are moving and deforming three-dimensional surfaces consisting of triangular faces.

valued, three-dimensional light-field, that represents the net strength of the illumination from all light sources at a particular position in space. Directions of light sources and orientations from surface elements are neglected. If the physical properties and arrangement of the light sources are known, better models for the light field may be constructed.

3. Results

We performed optical mapping imaging experiments with freely beating isolated rabbit hearts using a calibrated multi-camera optical mapping system filming the deforming ventricular wall during sinus rhythm. The deforming wall surface was reconstructed at high spatio-temporal resolutions over time in three spatial dimensions, firstly, by reconstructing the non-moving surface geometry of the electromechanically uncoupled heart and then by deforming the three-dimensional surface mesh according to multiple (2–4) sets of two-dimensional in-camera-plane displacement vector fields obtained via motion tracking when filming the contracting heart during electromechanical optical mapping.

Fig. 7 and 8 show reconstructed wall deformations and maps of action potential wave spread across the deforming three-dimensional ventricular surface of a rabbit heart during sinus rhythm. The data provides quantitative information on both the electrical and mechanical activity of the heart at high spatial and temporal resolutions (spatial resolution 0.4 mm , temporal resolution 2 ms). Fig. 7a) shows a rendering of a large part of the reconstructed three-dimensional deforming ventricular surface of the rabbit heart captured with 4 cameras. The geometry mesh consists of 2,286 vertices and 4,405 triangular faces that move through space as the heart deforms. The reconstructed area includes almost 180° of the circumference of the heart and the entire ventricular wall from apex to base. The rendering displays the tissue texture as seen by the 4 cameras during the optical mapping experiment under green illumination for excitation of the fluorescent dye and with fluorescence being emitted from the heart surface. The geometry mesh moves smoothly through space and deforms continuously (c.f. Fig. 8). As the tracking data was only minimally smoothed in space and time (see methods, section 2.5), the smooth and continuous motion demonstrates the robustness and accuracy of the tracking and moving wall shape reconstruction. Fig. 7b) shows the surface mesh composed of the vertices only. The motion of the entirety of vertices of the geometry mesh captures the motion and deformation of the heart wall surface during each heart beat (c.f. Fig. 8). Both panels a) and b) include three points (P1 blue, P2 red, P3 orange), from which the optical traces and corresponding activity are plotted in Fig. 7c). The left column in Fig. 7c) shows the raw, unprocessed optical traces obtained in one pixel that shows approximately the same physical position on the heart surface in three-dimensional space. The measured intensity fluctuates as the tissue moves back and forth. Due to the loss of correspondence between the pixel and the tissue location, the traces contain heavy motion artifacts. Even though the activity appears to be periodic, the characteristic action potential shape can not be identified. It does not even seem possible to be able to identify action potential upstrokes, which are usually very pronounced in optical traces and can be identified quite easily with moderate motion and mild motion artifacts. The modulations of the signal are in large parts due to motion, which occurs in synchrony with the repetitive electrical activation. The center column shows the registered and stabilized data, in which motion artifacts are in large parts suppressed or significantly reduced using the co-moving video analysis (see methods, section 2.7). The traces show the intensity modulations measured in one location on the tissue surface over time as it moves through space (for each point P1, P2 and P3).

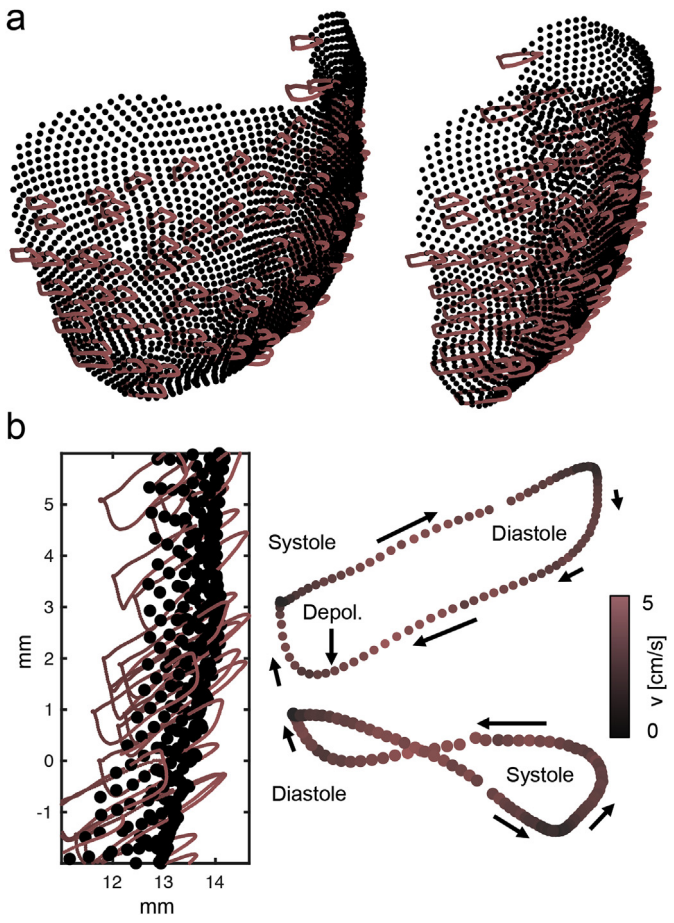

Fig. 8. Deforming heart surface and wall motion captured using electromechanical optical mapping during sinus rhythm (c.f. Fig. 7). **a)** Trajectories (red, displayed only every 20th trajectory) of mesh vertices (black) through 3D space during cardiac cycle. **b)** Elliptical trajectories aligned mostly in normal direction of epicardial surface describing back and forth movements of heart. Color-code (black-red) indicating instantaneous velocity of vertex along trajectory with highest velocities (5 cm/s) occurring along long sides of ellipses between systole and diastole (c.f. Fig. 9).

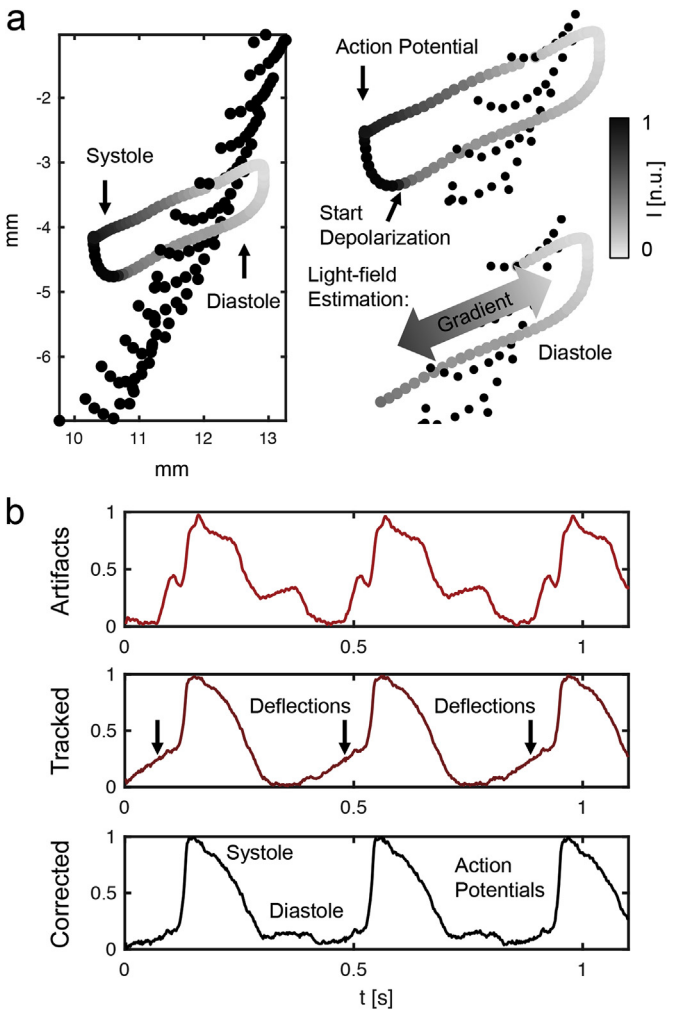

Fig. 9. Light-field correction for compensating motion artifacts caused by relative motion between tissue and illumination. **a)** Trajectory of single tissue vertex during cardiac cycle with intensity of imaged tissue segment over time along trajectory (normalized units [n.u] on interval [0 1]). During systole the intensity drops due to the depolarization of the action potential and an associated membrane-dependent and filtering-mediated drop in intensity on the detector. The lower subgraph shows the intensity along the trajectory only during the diastolic interval. Even along this part of the trajectory one can notice a gradient in the intensity likely due to a change in the illumination as the tissue moves through space. This gradient can be estimated in 3D space and then be used to correct the time-series accordingly. **b)** Effect of light-field correction onto optical trace. Upper graph shows raw unprocessed time-series with motion artifacts. Center graph shows times-series of same vertex after tracking and co-moving signal analysis but prior to light-field correction. Lower graph shows times-series after both tracking and co-moving signal analysis and light-field correction.

These intensity modulations were solely or in large parts caused by the action potential, given that the tracking and co-moving analysis (see section 2.7) and light-field correction (see section 2.8) removed the effects of optical flow and illumination changes or kept them minimal. In the co-moving frame, it is now possible to identify a sequence of action potentials with diastolic intervals in between the action potentials and the typical morphology of each individual action potential including its characteristic upstroke, plateau and repolarization. In particular, the traces show the characteristic assymmetry in the shape of the action potential with a steep upstroke and a pronounced diastolic interval rather than a sinusoidally shaped curve that is frequently seen in the uncompensated traces containing motion artifacts, see also Fig. 9b). Each tissue location corresponds to one vertex of the mesh shown in Fig. 7b). Accordingly, the full measurement data contains similar traces for almost all vertices of the geometry mesh shown in Fig. 7b), except for vertices close to the boundaries of the mesh where boundary effects decrease the quality of the tracking, reconstruction and artifact compensation (see also Supplementary Movie 2). From the moving vertex and co-moving time-series data it was then possible to compute maps of action potential wave spread on the deforming ventricular surface, see Fig. 7d). For comparison, the right column shows the optical traces from the surface of the non-moving, electromechanically uncoupled heart from the corresponding sites P1, P2 and P3. The traces were obtained about 15 min later after the effective removal of any contractile motion using Blebbistatin. The time-series show action potentials without any noticeable motion artifacts. Comparing these quasi-perfect optical traces obtained from the static, non-moving heart with the compensated motion-stabilized traces, it can be concluded that the traces from the strongly moving and deforming heart yet contain noticeable motion artifacts, in particular, in the form of deflections during the diastolic interval. However, action potentials are sufficiently well recovered and at no time obscured, such that it becomes possible to perform activation time measurements or reconstructing maps of wave propagation across

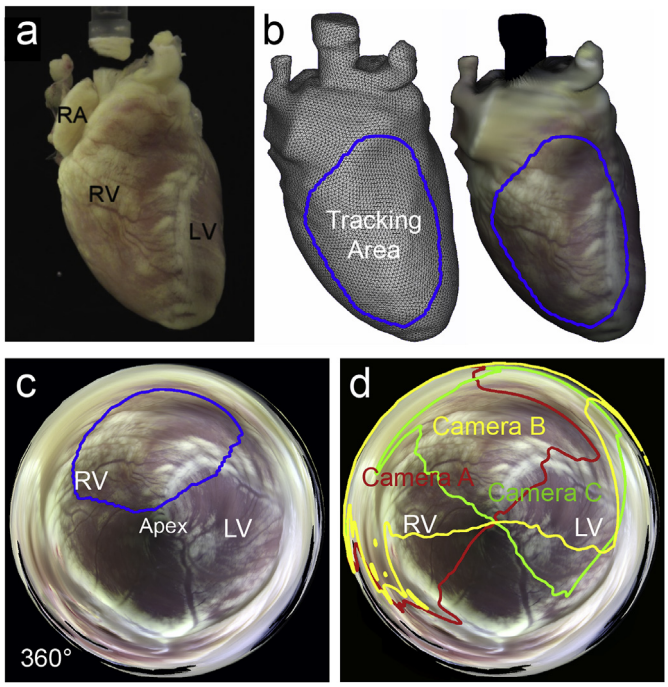

Fig. 10. 3D surface reconstruction of rabbit heart #1 using 3 cameras. **a)** Photograph of rabbit heart in perfusion bath. **b)** Reconstructed, high-resolution triangular mesh rendered as wireframe (left) and with color texture map (right). Blue outline indicates surface region, for which 3D deformation tracking was applied. **c)** Polar color texture map of entire heart surface, generated from projection of 72 photographs onto the mesh. Blue outline indicates Tracking Area as in panel b. **d)** Polar texture map with outlines of field of views of three cameras, which were arranged at 45° looking through adjacent windows of an 8-sided bath.

the deforming heart surface. Action potentials could be recovered from almost the entire reconstructed surface. Fig. 7d) shows the corresponding maps of action potential wave spread across the deforming ventricular surface (see also Supplementary Movie 2). The first image shows the heart surface during the diastolic interval approximately 140*ms* before the depolarization of the tissue. The course of the action potential is displayed in normalized units ([n.u.]), with the time-series being normalized individually by their minimal and maximal values over time, the resulting normalized time-series being flipped or inverted (all activity is mapped onto the interval [0 1]). Accordingly, the undepolarized tissue surface is shown in black. The second image shows the heart surface during the depolarization of the ventricular muscle during sinus activation. Accordingly, depolarized tissue is shown in white. The ventricular muscle is activated almost instantaneously everywhere on its surface. At the same time, the heart surface is visibly deformed compared to its shape and mechanical configuration in the left image. The dashed line is a reference line that is supposed to facilitate viewing of the motion and deformation of the tissue. The mechanical configuration of the mesh and its evolution over time captures non-rigid deformations as well as rigid body or translational motion and rotations. The maps are moving and deforming three-dimensional surfaces in three-dimensional space consisting of triangular faces defined by 3 vertices. The right image shows a later phase of the action potential shortly before or during the repolarization of the muscle about 60*ms* after the upstroke of the action potential. The image data shows a homogeneous map of the action potential wave, but yet contains residual motion artifacts (see also Supplementary Movie 2).

Supplementary video related to this article can be found at https://doi.org/10.1016/j.pbiomolbio.2017.09.015.

The motion and mechanical deformation of the wall surface captured during the electromechanical optical mapping experiment is depicted in Fig. 8. Fig. 8a) shows the vertex mesh (black dots) of the same heart as depicted in Fig. 7 and the trajectories (red lines) of some of their vertices (every 20th vertex from the unstructured vertex grid). The trajectories exhibit an elliptical shape, the main axis of the ellipses being aligned in normal direction to the tissue surface, the entirety of trajectories describing a translational back and forth movement of the tissue surface in radial direction of the heart, see Fig. 8b). The heart moves approximately 3*mm* back and forth, which is in the order of $15-20\%$ of its diameter (see also Supplementary Movies 1 and 2 for an impression of the strong movements and contractions). The motion corresponds to a movement in and out of the image plane in Fig. 7d). The ellipses are closed and collapse onto each other over many cardiac cycles (we measured up to 5 s), indicating that the motion of the heart is very regular and similar over the different cardiac cycles. Fig. 8b) shows that in addition to the trajectory it is also possible to compute and display the velocity of each vertex along its trajectory. The color-code (black-red) indicates the strength of the instantaneous velocity of the vertex along its trajectory, the highest velocities ($5cm/s$) occurring along the long sides of ellipses between systole and diastole during translational motion of the entire heart (c.f. Fig. 9).

Fig. 9 shows the efficacy of the light-field correction for compensating motion artifacts caused by relative motion between tissue and light sources and related illumination changes, see also section 2.8. We found that the light-field correction could significantly improve the quality of the recovery of action potentials from parts of the surface of strongly moving and deforming hearts during electromechanical optical mapping. As an additional post-processing step after the tracking and motion stabilization procedure, the light-field correction enabled to recover action potentials from heavily distorted optical traces and enhanced action potential morphology, see Fig. 9b). We estimated the local light-field or effective illumination intensity around each vertex from the residual intensity fluctuations during the diastolic interval. Fig. 9a) shows the trajectory of a single tissue vertex during the full cardiac cycle. The intensity of the imaged tissue segment that was measured over time along the trajectory is shown in normalized units (black-and-white color code, [n.u]). During systole, the intensity drops abruptly with the depolarization of the action potential, which produces due to membrane-dependent emission spectrum shifts and the bandpass filtering a drop in intensity on the detector (black part of the trajectory). During diastole, we would expect the the intensity to be constant if the tracking of the tissue segment through space was accurate and effects of optical flow were minimized. However, we consistently observed a gradient in intensity suggesting that the illumination changes whenever the tissue moves along the direction of an illumination gradient. Using the intensity data from the trajectory and its neighbouring trajectories during the diastolic interval, we estimated the effective intensity distribution or light-field using equation (12) and corrected the traces accordingly. The effect of the light-field correction onto the optical traces is shown in Fig. 9b). The raw unprocessed optical trace containing heavy motion artifacts is shown in the upper time-series. The graph in the central panel corresponds to the times-series after tracking and the co-moving signal analysis but prior to the light-field correction. It can be noticed that the trace appears to contain positive deflections prior to the upstroke of the action potential. The lower graph shows the times-series after both tracking and the co-moving signal analysis and the light-field correction. With the light-field correction, the positive deflections disappeared, leading to a more abrupt action potential upstroke

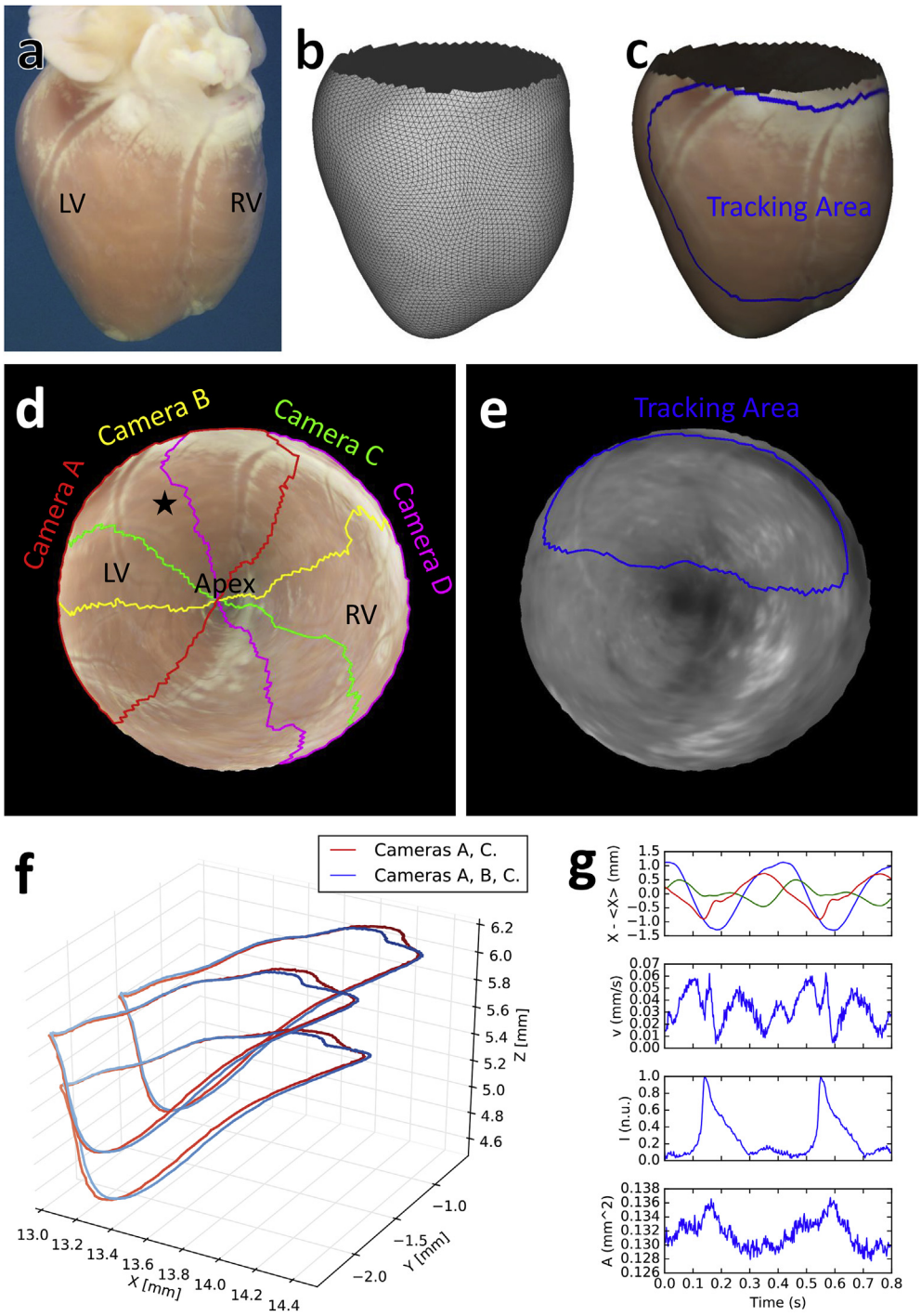

Fig. 11. 3D surface reconstruction of rabbit heart #2 using 4 cameras. **a)** Photograph of rabbit heart in perfusion bath. **b)** Reconstructed, high-resolution triangular mesh of the ventricles rendered as wireframe. **c)** Triangular mesh rendered with color texture map. Blue outline indicates surface region, for which 3D deformation tracking was applied. **d)** Polar color texture map of the ventricular surface, generated from projection of 72 photographs onto the mesh. Outlines show field of views of four cameras, which were arranged at 45° looking through adjacent windows of an 8-sided bath. **e)** Polar fluorescence texture map of the ventricular surface, generated from projection of 72 images of the rotating heart with camera B under green illumination. Blue outline indicating Tracking Area as in panel c. **f)** Comparison of reconstructed trajectories of three vertices of a triangle face reconstructed using two (red) or three (blue) cameras, arranged at 90° or 45°, respectively. The location of the triangle is indicated by a black star in panel d. **g)** Plot of time series of triangle shown in panel f. First row: X (blue), Y (green), and Z (red) coordinates around mean position of first triangle point. Second row: velocity of first triangle point. Third row: corrected fluorescence intensity at first triangle point. Fourth row: Surface area of triangle.

and a flat diastolic interval in between the action potentials.

During the electromechanical optical mapping experiment, large parts of the heart are not visible by any of the high-speed cameras and only parts, which can be seen by at least two cameras can be tracked in three-dimensional space. The deforming ventricular wall surface, which is shown in Fig. 7a), and on which we measured electrical and mechanical data at high spatial and temporal resolutions, is only part of a larger 360° reconstruction of

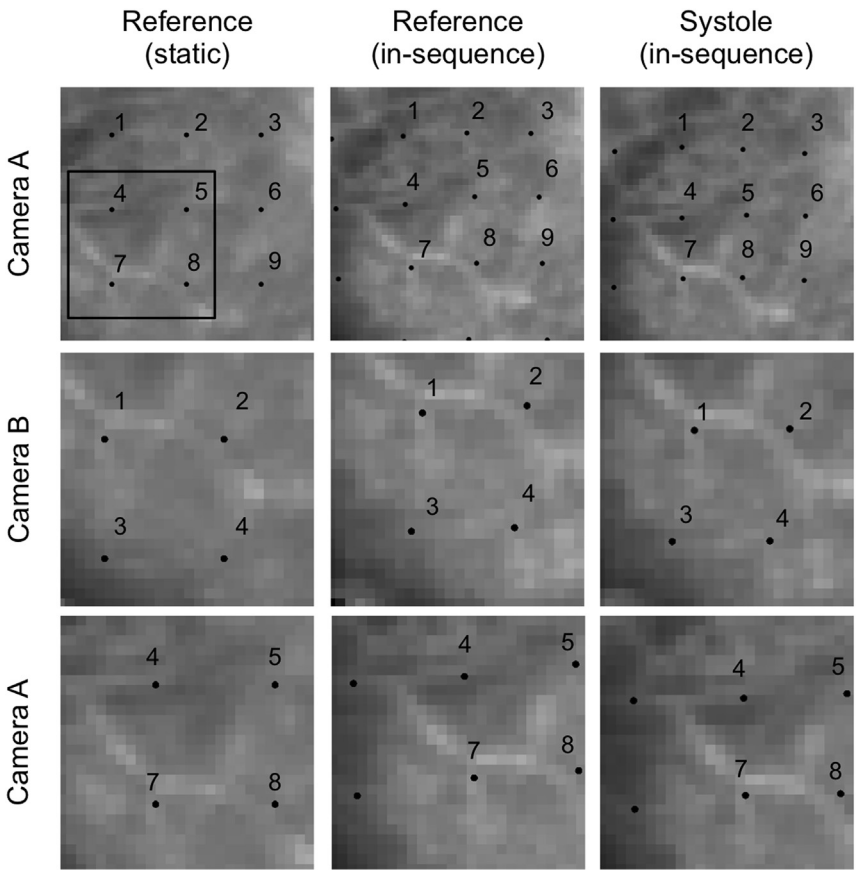

Fig. 12. Efficacy of tracking tissue motion in optical mapping videos. Image registration algorithm tracks tissue landmarks, features or texture through the image plane, here shown for three exemplary sequences in each row: the first column shows the uncoupled tissue at the end of the experiment, the second and third columns show the tissue during the electromechanical optical mapping experiment during diastole and systole. The black dots (part of a regular grid, every 10th data point is shown) indicate examplary tissue segments, which are being tracked through the video images with respect to the reference configuration. The tracked shifts can be verified by simple visual inspection.

the entire surface of the uncoupled heart. Figs. 10 and 11 show the full 3D reconstruction of two different hearts, one imaged with 3 cameras (10) and one imaged with 4 cameras (11, 7) during electromechanical optical mapping. For both hearts, the entire static surface geometry of the heart was reconstructed optically using the same methodology as described in section 2.6 at the end of each experiment after the administration of Blebbistatin. However, the comparison of Figs. 10 and 11 illustrates the difference that using 3 or 4 cameras in the optical mapping experiment make onto the size of the dynamically reconstructed deforming heart wall. Figs. 10a) and 11a) show a photograph of a rabbit heart hanging inside the perfusion bath, the photograph being taken from a similar perspective through the glass walls of the aquarium as from which it was filmed with one camera. Fig. 10b) 11 b-c) show the three-dimensional reconstruction of the outer shape of the non-moving, electromechanically uncoupled heart as a triangular mesh, rendered both as a wireframe model (left) and with color texture map applied (right). As described in the methods section, the entire surface geometry including the ventricles, atria and aorta was reconstructed optically at the end of the experiment after the administration of Bebbistatin by rotating the heart. The triangular mesh indicates the high spatial resolution (Fig. 10: 23,550 faces, 0.16 mm^2 average surface area per face) of the surface reconstruction. In both Figs. 10 and 11, the morphological configuration of the heart corresponds to the electromechanically uncoupled, non-moving configuration χ_s of the heart at the end of the experiment ($15-20$ minutes, see also Fig. 3b), as the three-dimensional shape reconstruction could only be performed with non-moving hearts. The area enclosed by the blue line indicates the area on the ventricular surface, which was filmed during the electromechanical optical mapping part of the experiment with 3 or 4 cameras respectively, and for which tissue displacement data and optical maps could be computed. The area in Fig. 10 is smaller than in Fig. 11 as it was only filmed with 3 cameras instead of with 4 cameras. Fig. 10c) shows the corresponding area in one polar texture map of the entire ventricular surface obtained from 72 photographs of the heart during the 360° rotation projected onto the reconstructed geometry and blended together, the entire epicard surface being shown in one image with the apex at the center of the image. Correspondingly, Fig. 11e) shows the tracking area in a polar map obtained from 72 video images from the high-speed cameras during the rotation. The reconstructed deforming area of the heart filmed with 4 cameras is substantially larger than from the one filmed with 3 cameras and corresponds to almost 180° of the surface of the heart. Fig. 10d) shows the the same polar texture map as in 10c), however, the three fields of view of the three high-speed cameras A, B and C are displayed on top of the map as red, yellow and green lines respectively. The right ventricular wall is covered partially by the field of view of camera A, parts of both the right and left ventricular walls are covered by camera B and the left ventricular wall is covered by camera C. At 45° camera angle, there is a large overlap in the fields of view of the cameras and, in particular, there is a region in which all three fields of view overlap. The same degree of overlap is achieved in Fig. 11d) and with 4 cameras only a small part of the ventricles at the bottom of the map between the pink and red line can not be observed by any of the

cameras. This suggests that the entire heart could presumably be observed by 6 cameras. Nevertheless, for the computation of the dynamically deforming meshes of both hearts it was necessary that at least two of the fields of view of 2 of the high-speed cameras overlapped. Accordingly, in Fig. 11d) only the region in the upper half of the map between the yellow and the green line could be used to reconstruct three-dimensional wall motion. The effective tracking area enclosed by the blue line shown in Fig. 11e) corresponds approximately to this area and is only slightly smaller because some of the vectors close to the boundaries of the fields of view were discarded.

Texture maps as shown in Fig. 10c) or Fig. 11d) can be computed at arbitrarily high resolutions. Due to the high resolution of the DSLR camera, the color texture map can also be computed at high resolution. Even at a resolution of just 1024×1024 pixels as shown here, the detail provided by the texture map exceeds the resolution of the triangular mesh, meaning that each triangular face of the mesh contains a texture patch that may consist of multiple pixels of the original photograph, resulting in almost photo-realistic rendering of the textured mesh. From the photographs and color texture it is possible to identify anatomical structures on the heart surface and to compare them to the activity in the optical maps. For instance, in the color texture map one can easily identify the left descending artery, which separates the right and the left ventricle.

The efficacy of tracking motion in the two-dimensional video data is demonstrated in Fig. 12. The image registration algorithm tracks tissue landmarks, features or texture through the image plane and was used to determine shifts of the tissue in the contrast-enhanced video images (c.f. Fig. 4). The figure contains 3×3 panels with video images showing the same part of the heart surface as seen from one of the cameras. The first row shows a close-up of the video image from camera A, the second row shows a close-up of the video image from camera B, and the third row shows an enlargement of the first row. The first column shows the tissue at the end of the experiment in its reference configuration χ_s. The second and third columns show the tissue approximately $15-20$ minutes earlier during the electromechanical optical mapping part of the experiment during diastole and systole, respectively. The second column shows the tissue in the reference configuration χ_r in the reference frame I_r or C_r respectively within the sequence. The black dots indicate tissue segments (subsampled from a regular grid with higher resolution), which are being tracked with respect to the reference configuration in the static reference frame I_s or C_s respectively and through the sequence of video images $I_1, \ldots, I_N$ (or $C_1, \ldots, C_N$). Notice that the heart surface seen in the video images in the first column appears differently than the video images in the second and third columns. In particular, the texture of the tissue in the video images in the second and third columns is much more similar, because the images were acquired within a short time, typically within a few hundreds of milliseconds or seconds. In contrast, the video images in the first column were acquired $15-20$ minutes later. During this time, the heart's visual appearance was changed significantly, likely due to photo-bleaching, washout or redistribution of the fluorescent dye or administering of Blebbistatin. The figure demonstrates that the motion tracking algorithm and scheme, see Fig. 5b), was nevertheless able to relate the video images to each other and to detect shifts in between all images reliably. Nevertheless, the differences in the visual appearance in between the instantaneous video images $I_1, \ldots, I_N$ (or $C_1, \ldots, C_N$) and the static reference video image I_s (or C_s), caused the tracking to be insufficiently robust if the scheme shown in Fig. 5b) had not been applied, but rather the shifts were aimed to be computed in between each video image $I_1, \ldots, I_N$ and the reference image I_s directly, as in Fig. 5a). For the tracking to work reliably, it was necessary to warp all instantaneous video images to the in-sequence reference configuration χ_r and then to register all warped images $\tilde{I}_1, \ldots, \tilde{I}_N$ with respect to the static reference image I_s to obtain an averaged map for the deformation that occurred during administering of Blebbistatin.

4. Discussion

We demonstrated that optical mapping can be performed with beating, strongly contracting hearts and that action potential waves can be visualized on the three-dimensional deforming ventricular wall as the heart contracts during sinus rhythm. In particular, we demonstrated that movements and deformations of the heart surface can be captured at high spatial resolutions without markers being attached to the heart. We used an approach, in which at first the beating heart was filmed with multiple calibrated cameras and, afterwards, as the heart's motion was suppressed using uncoupling agents, the immobilized heart's geometry was reconstructed, which then could be deformed according to the tracking data obtained while filming the beating heart. This approach is fundamentally different from another approach reported by Zhang et al. (2016), in which heart wall shapes and wall movements were tracked and reconstructed immediately and directly using the video image data only, while relying on the use of markers attached to the heart surface. Moreover, we demonstrated that it is possible to use a purely numerical approach to compensate motion artifacts, which are related to inhomogeneous illumination and relative motion between the heart and the light sources. Our approach has a series of advantages and disadvantages.

One of the main advantages of our approach is that we did not have to use markers and that the heart's outer shape could be reconstructed at very high spatial resolutions independently of any given number of markers, the spatial resolution being limited only by the spatial resolution of the high-speed cameras and the tracking of the video images. As the tracking was conducted in each pixel, we obtained essentially the same resolution given by the detector of the high-speed cameras (128×128 pixels). At the same time, the optical three-dimensional geometry reconstruction provided even higher spatial resolutions than the projected pixel sizes of the high-speed cameras. Each vertex of the geometry mesh was displaced using data from multiple cameras. While Zhang et al. (2016) relied on markers in order to obtain corresponding pairs of tissue coordinates in two cameras, our approach provided such corresponding pairs automatically as it associated two corresponding pairs via the readily existing mesh of the reconstructed surface geometry, see Fig. 6.

Another advancement in our approach is the introduction of the numerical removal or inhibition of motion artifacts caused by inhomogeneous illumination and relative motion between tissue and light sources using a light-field correction, see section 2.8 and Fig. 9. The technique achieves similarly as ratiometric imaging a reduction of baseline drifts which are independent of dissociation effects. Therefore, it could be used as a complementary technique in conjunction with ratiometric imaging or presumably also as a stand-alone solution. However, further research would be required to systematically evaluate the technique's performance for various situations and in comparison to ratiometric imaging. At the moment, we are unaware of how different movements of the heart (see trajectories in Fig. 9) affect the quality of the light-field estimation. It is important to note at this point, that the light-field correction did not always improve the action potential shape as shown in Fig. 9b). In many cases (approx. 50%), it did not have a noticeable effect onto the traces and in some fewer cases it even seemed to decrease the quality of the recovery. However, this could

be due to the particularly regular motion of the heart and relatively restricted volume around each vertex, from which we were able to sample the intensity distribution caused by the light-field. The very regular motion of the heart restricted us to sampling along the elliptical trajectories in a quasi two-dimensional plane. In situations with less regular motion, the trajectories would presumably be more complex and allow volumetric sampling, which could in turn improve the quality of the light-field estimation. In principle, the light-field correction could also be used to compensate motion artifacts during arrhythmic activity. However, due to the absence of a diastolic interval during arrhythmic activity, the light-field correction would have to be modified in that the whole trajectories including intensity modulations caused by the action potential would have to be used in the sampling process. Then sampling over long times could average out the contributions by the action potential. Alternatively, the light-field could be estimated prior to staining with fluorescent dye, recording movements of the heart surface and probing baseline drifts for various shifts of the tissue without the heart emitting fluorescence. In principle, light-field correction could also be used with 2D video data.

In our experiments the 8-sided bath limited us to camera positions of 45° or 90°. Fig. 11f) compares the trajectories of a triangle reconstructed with three cameras arranged at consecutive 45° positions versus just two cameras positioned at 90°. The reconstructed trajectories do not differ much, suggesting that separations larger than 45° can also be used for 3D deformation tracking. However, with our current approach it would not be sufficient to use four cameras arranged at 90° for panoramic tracking of the whole 360° heart surface, because the usable overlap between two cameras is currently limited in our approach due to lacking 2D tracking data at the boundaries between heart and background, as described in section 2.7. We anticipate that full 360° panoramic 3D deformation tracking should be possible with 6 cameras using our technique. If cameras with a higher spatial resolution were used, then even 5 cameras might be sufficient. Fig. 11g) shows reconstructed time-series for this triangle. Position, velocity and corrected fluorescence are plotted for the first point of the triangle. The last row in Fig. 11g) shows the surface area of this triangle and illustrates how the reconstructed mechanical motion can be processed further.

One of the major drawbacks of our approach is the long delay (10 – 15 minutes) between the electromechanical optical mapping experiment and the reconstruction of the three-dimensional geometry of the heart at the end of the experiment. The relatively long delay time is required to administer Blebbistatin and to wait for the uncoupling agent to become effective, because the outer shape reconstruction is a lengthy process (5 – 8 minutes), involves the 360° rotation and taking photographs of the heart and can only be performed with non-moving hearts. The long delay time is problematic for two reasons: on the one hand the heart's visual appearance can change in that time to a degree that the tracking between the fluorescence video images acquired during the reconstruction and the video image sequence acquired during optical mapping becomes compromised, see Figs. 4b) and 12. To overcome this problem we had to introduce the tracking scheme presented in Fig. 5b). On the other hand, one can often have the situation that the heart's size and volume increases significantly (length changes in the order of a few percent), which prohibits further analysis of the experimental data. We experienced significant volume changes and swelling, such that in 2 out of 4 experiments, which we performed overall, it became immediately clear after the experiment that we could not analyze the data. The heart's size and volume increased in both the time in which Blebbistatin was administered as well as in the time that was required to perform the 360° rotation of the heart for the geometry reconstruction (72 photographs, 5 – 8 minutes), likely due to osmotic pressure. In cases in which the heart size changed mildly but reconstruction was yet considered possible, the analysis contained systematic errors due to the mismatches of silhouettes that may have gotten included in the geometry reconstruction. Particularly, shape changes during which either the heart elongated along an arbitrary axis deviating from the vertical rotational axis, or during which the heart moved out of the field of view of one of the cameras were prohibiting further analysis.

We performed the entire experiment in relatively short times of typically less than 30 min to minimize the above mentioned effects. To avoid critical shape changes of the heart during reconstruction, it would be advantageous to decrease the time that is necessary to perform the optical reconstruction down to a few seconds. Generally, it could be possible to compensate undesired heart volume increase pharmacologically, yet, we did not test this option. We also did not verify whether the dynamic reconstruction of the three-dimensional geometry of the heart could be performed after several hours of the experiment. It could be a challenge in this case to be able to register and relate the video data with the video data that was acquired several hours earlier. A solution could be to perform multiple recordings and registrations in the meantime and stitching such registrations together, to ultimately register deformations that occurred in between longer periods of time. We are aware that the time constraints imposed by the geometry reconstruction constitute a serious limitation as optical mapping experiments can last for up to several hours and are typically also performed over several hours. Of course, in general, the problems associated with uncoupling the heart electromechanically for shape reconstruction and the long delay times that come with that procedure could be circumvented by using panoramic imaging or stereo imaging approaches, in which the deforming surface is captured instantaneously.

Ground truth data of the actual, instantaneous deformation of the epicardial surface, to which the reconstructed three-dimensional deformation could have been compared to, was not available in the experiments. Therefore, the quality of the reconstruction method and their results could only be inferred from the efficacy of motion-artifact-removal. Co-moving time series depicted in Fig. 7c) show drastically reduced motion artifacts. Residual artifacts were partly caused by incomplete motion-compensation or light-field correction. This issue could be addressed with different experimental methodology, e.g. additional ratiometric optical mapping, or with numerical post-processing like high-pass filtering.

The strength of our method lies in the easy experimental execution and the simplicity of the numerical, two- and three-dimensional tracking and reconstruction procedures described in sections 2.5 and 2.7. Nonetheless, there are several possibilities for improvements. The weight $w_{k,m}$ for summation of the quadratic differences in equation (5) was set to zero for angles $\varphi > \widehat{\varphi} = 80°$. This limit was chosen, because the optical flow cannot be computed accurately at the border of the heart, where the angle of observation is near 90°, due to inference with the static background. The hard limit $\widehat{\varphi}$ could be replaced by an additional multiplicative factor, describing the quality of the displacement vector field $\mathbf{u}_k^t$ at each pixel. Furthermore, this simple formula should be extended, such that possible occlusions of the geometry with itself are respected, and the normal vector $\mathbf{N}_m$ be recomputed for every time t.

5. Conclusions

We demonstrated that it is possible to perform panoramic optical mapping experiments with beating hearts. Motion and deformations of hearts could be reconstructed at high spatial

resolutions using numerical image registration and motion tracking techniques. Maps of action potential wave spread across the deforming surface could be visualized with significantly reduced motion artifacts. The future of optical mapping will be mapping freely beating and contracting hearts.

Acknowledgements

We would like to thank M. Kunze, D. Hornung and C. Richter for technical assistance. The research leading to the results has received funding from the German Research Foundation (to S.L.), the Collaborative Research Center SFB 1002 'Modulatory Units in Heart Failure' (to S.L and J.C), the Collaborative Research Center SFB 937 'Collective Behavior of Soft and Biological Matter' (to S.L and J.C), the German Center for Cardiovascular Research (DZHK e.V., partnersite Göttingen) (to S.L.), and the Max Planck Society (to S.L.).

Supplementary material

Two supplementary movie files are available online. Supplementary movie 1 shows the reconstructed triangular mesh of the heart surface as well as the three-dimensional deformation of the tracked area of the contracting heart #1 during sinus rhythm. Supplementary movie 2 shows the same for heart #2, and additionally shows the projected and normalized fluorescent membrane potential before and after applying the light field correction.

References

Bachtel, A.D., Gray, R.A., Rogers, J.M., 2011. A novel approach to dual excitation ratiometric optical mapping of cardiac action potentials with di-4-anepps using pulsed led excitation. IEEE Trans. Biomed. Eng. 58, 2120–2126.

Baker, L.C., Wolk, R., Choi, B.-R., Watkins, S., Plan, P.P., Shah, A., Salama, G., 2004. Effects of mechanical uncouplers, diacetyl monoxime, and cytochalasin-d on the electrophysiology of perfused mouse hearts. Am. J. Physiol. Heart Circ. Physiol. 287, H1771–H1779.

Bourgeois, E.B., Bachtel, A.D., Huang, J., Walcott, G.P., Rogers, J.M., 2011. Simultaneous optical mapping of transmembrane potential and wall motion in isolated, perfused whole hearts. J. Biomed. Opt. 16.

Brack, K.E., Narang, R., Winter, J., André, N.G., 2013. The mechanical uncoupler blebbistatin is associated with significant electrophysiological effects in the isolated rabbit heart. Exp. Physiol. 98 (5), 1009–1027.

Brandes, R., Figueredo, V.M., Comacho, S.A., Masie, B.M., Weiner, W.M., 1992. Suppression of motion artifacts in fluorescence spectroscopy of perfused hearts. Am. J. Physiol. Heart Circ. Physiol. 263, 972–980.

Choi, B.R., Salama, G., 2000. Simultaneous maps of optical action potentials and calcium transients in Guinea-pig hearts: mechanisms underlying concordant alternans. J. Physiol. 529, 171–188.

Choi, P.T., Lam, K.C., Lui, L.M., 2015. Flash: fast landmark aligned spherical harmonic parameterization for genus-0 closed brain surfaces. SIAM J. Imaging Sci. 8 (1), 67–94. http://epubs.siam.org/doi/abs/10.1137/130950008.

Christoph, J., 2015. Intramural Visualization of Scroll Waves in the Heart. Georg-August-University Göttingen. http://hdl.handle.net/11858/00-1735-0000-0023-9642-D.

Cignoni, P., Callieri, M., Corsini, M., Dellepiane, M., Ganovelli, F., Ranzuglia, G., 2008. MeshLab: an open-source mesh processing tool. In: Scarano, V., Chiara, R.D., Erra, U. (Eds.), Eurographics Italian Chapter Conference. The Eurographics Association.

Davidenko, J.M., Pertsov, A.V., Salomonsz, R., Baxter, W., Jalife, J., 1992. Stationary and drifting spiral waves of excitation in isolated cardiac muscle. Nature 355, 349–351.

Efimov, I.R., Nikolski, V.P., Salama, G., 2004. Optical imaging of the heart. Circ. Res. 95, 21–33.

Efimov, I.R., Rendt, J.M., Salama, G., 1994. Optical maps of intracellular [ca2+]i transients and action-potentials from the surface of perfused Guinea-pig hearts. Circulation 90.

Fedorov, V., Lozinsky, I., Sosunov, E., Anyukhovsky, E., Rosen, M., Balke, C., Efimov, I., 2007. Application of blebbistatin as an excitation-contraction uncoupler for electrophysiologic study of rat and rabbit hearts. Heart rhythm. 4, 619–626.

Gray, R.A., Pertsov, A.M., Jalife, J., 1998. Spatial and temporal organization during cardiac fibrillation. Nature 392, 75–78.

Gwathmey, J.K., Hajjar, R.J., Solaro, R.J., 1991. Contractile deactivation and uncoupling of crossbridges: effects of 2,3-butanedionemonoxime on mammalian myocardium. Circ. Res. 69, 1280–1292.

Herron, T.J., Lee, P., Jalife, J., 2012. Optical imaging of voltage and calcium in cardiac cells and tissues. Circ. Res. 110, 609–623.

Hooks, D.A., LeGrice, I.J., Harvey, J.D., Smaill, B.H., 2001. Intramural multisite recording of transmembrane potential in the heart. Biophys. J. 81, 2671–2680.

Itseez/Intel, USA, 2015. OpenCV 3.1.0 – documentation of camera calibration. http://docs.opencv.org/3.1.0/d9/d0c/group__calib3d.html.

Jalife, J., Gray, R., 1996. Drifting vortices of electrical waves underlie ventricular fibrillation in the rabbit heart. Acta Physiol. Scand. 157, 123–131.

Kay, M.W., Amison, P.M., Rogers, J.M., 2004. Three-dimensional surface reconstruction and panoramic optical mapping of large hearts. IEEE Trans. Biomed. Eng. 51, 1219–1229.

Kay, M.W., Efimov, I., 2016. Optical mapping of cardiac electromechanics. Biophysical J. 111 (2), 269–270.

Kazhdan, M., Hoppe, H., 2013. Screened poisson surface reconstruction. ACM Trans. Graph. (TOG) 32 (3), 29.

Khwaounjoo, P., Rutherford, S.L., Svrcek, M., LeGriece, I.J., Trew, M.L., Smaill, B.H., 2015. Image-based motion correction for optical mapping of cardiac electrical activity. Ann. Biomed. Eng. 43, 1235–1246.

Knisley, S.B., Justice, R.K., Kong, W., Johnson, P.L., 2000. Ratiometry of transmembrane voltage-sensitive fluorescent dye emission in hearts. Am. J. Physiology - Heart Circulatory Physiology 279 (3), 1421–1433.

Laughner, I.J., Zhang, S., Efimov, I.R., 2012. Mapping cardiac surface mechanics with structured light imaging. Am. J. Physiol. Heart Circ. Physiol. 303, 712–720.

Laurita, K.R., Girouard, S.D., Akar, F.G., Rosenbaum, D.S., 1998. Modulated dispersion explains changes in arrhythmia vulnerability during premature stimulation of the heart. Circulation 98, 2773–2780.

Lee, M.H., Lin, S.F., Ohara, T., Omichi, C., Okuyama, Y., Chudin, E., Garfinkel, A., Weiss, N.J., Karagueuzian, H.S., Chen, P.S., 2001. Effects of diacetyl monoxime and cytochalasin d on ventricular fibrillation in swine right ventricles. Am. J. Physiology - Heart Circulatory Physiology 280 (6), 2689–2696.

Lee, P., Bollensdorff, C., Quinn, T.A., Wuskell, J.P., Loew, L.M., Kohl, P., 2011. Single-sensor system for spatially resolved, continuous, and multiparametric optical mapping of cardiac tissue. Heart rhythm. 8 (9), 1482–1491.

Li, T., Sperelakis, N., Teneick, R.E., Solaro, J.R., 1985. Effects of diacetyl monoxime on cardiac excitation-contraction coupling. J. Pharmacol. Exp. Ther. 232, 688–695.

Lou, Q., Wenwen, L., Efimov, I.R., 2012. The role of dynamic instability and wavelength in arrhythmia maintenance as revealed by panoramic imaging with blebbistatin vs. 2,3-butanedione monoxime. Am. J. Physiol. Heart Circ. Physiol. 302, 262–269.

Morad, M., Salama, G., 1979. Optical probes of membrane potential in heart muscle. J. Physiol. Lond. 292, 267–295.

Nanthakumar, K.J.J., Mass, S., Downar, E., Pop, M., Asta, J., Ross, H., Rao, V., Mironov, S., Sevaptsidis, E., Rogers, J., Wright, G., Dhopeshwarkar, R., 2007. Optical mapping of langendorff-perfused human hearts: establishing a model for the study of ventricular fibrillation in humans. Am. J. Physiol. Heart Circ. Physiol. 293, 875–880.

Niem, W., 1994. Robust and fast modelling of 3D natural objects from multiple views. SPIE proceedings 2182. Image Video Process. II 388–397.

Periaswamy, S., Weaver, J., Healy, D., Rockmore, Kostelec, P., Farid, H., 2000. Differential affine motion estimation for medical image registration. Wavelet Appl. Signal Image Process. 8.

Pertsov, A.M., Davidenko, J.M., Salomensz, R., Baxter, W.T., Jalife, J., 1993. Spiral waves of excitation underlie reentrant activity in isolated cardiac muscle. Circ. Res. 72, 631–650.

Pietroni, N., Tarini, M., Cignoni, P., 2010. Almost isometric mesh parameterization through abstract domains. IEEE Trans. Vis. Comput. Graph. 16 (4), 621–635.

Qu, F., Ripplinger, C.M., Nikolski, V.P., Grimm, C., Efimov, I.R., 2007. Three-dimensional panoramic imaging of cardiac arrhythmias in rabbit heart. J. Biomed. Opt. 12.

Riccio, M.L., Koller, M.L., Gilmour, R.F., 1999. Electrical restitution and spatiotemporal organization during ventricular fibrillation. Circulation Res. 84 (8), 955–963. http://circres.ahajournals.org/content/84/8/955.

Rodriguez, M., Nygren, A., 2012. Application of scale-space descriptors for the reliable detection of keypoints for image registration in optical mapping studies in whole heart preparations. Proc. IEEE Eng. Med. Biol. Soc. 3171–3174.

Rodriguez, M.P., Nygren, A., 2015. Motion estimation in cardiac fluorescence imaging with scale-space landmarks and optical flow: a comparative study. IEEE Trans. Biomed. Eng. 62, 774–782.

Rogers, J.M., Walcott, P.G., Gladden, J.D., Melnick, S.B., Kay, M.W., 2007. Panoramic optical mapping reveals continuous epicardial reentry during ventricular fibrillation in the isolated swine heart. Biophysical J. 92, 1090–1095.

Rohde, G.K., Benoit, B.M., Lin, S., 2005. Corrections of motion artifacts in cardiac optical mapping using image registration. IEEE Trans. Biomed. Eng. 52, 338–341.

Salama, G., 2001. Optical mapping: background and historical perspective. In: Rosenbaum, D., Jalife, J. (Eds.), Optical Mapping of Cardiac Excitation and Arrhythmias. Futura Publishing Company, Inc, Armonk, NY.

Salama, G., Lombardi, R., Elson, J., 1987. Maps of optical action potentials and nadh fluorescence in intact working hearts. Am. J. Physiol. 252, 384–394.

Salama, G., Morad, M., 1976. Merocyanine 540 as an optical probe of transmembrane electrical activity in the heart. Science 191, 485–487.

Stender, B., Ernst, F., Wang, B., Zhang, Z.X., Schlaefer, A., 2013. Motion Compensation of Optical Mapping Signals from Isolated Beating Rat Hearts.

Svrcek, M., Chen, A., Rutherford, S., Sekora, J., Provaznik, I., Smaill, B., 2010. Suppressing motion artifact in cardiac electrical optical mapping. In: Conference Proceedings, Analysis and IMAGES.

Svrcek, M., Rutherford, S., Smaill, B., 2009. Characteristics of motion artifacts in

cardiac optical mapping studies. In: Conference Proceedings, 31st Annual International Conference of the IEEE EMBS, vol. 31, pp. 3240–3243.
Swift, L.M., Asfour, H., Posnack, N.G., Arutunyan, A., Kay, M.W., Sarvazyan, N., 2012. Properties of blebbistatin for cardiac optical mapping and other imaging applications. Pflugers Arch. 464 (5), 503–512.
Tai, D.C.-S., Caldwell, B.J., LeGrice, I.J., Hooks, D.A., Pullan, A.J., Smaill, B.H., 2004. Correction of motion artifact in transmembrane voltage-sensitive fluorescent dye emission in hearts. Am. J. Physiol. Heart Circ. Physiol. 287, 985–993.
Witkowski, F.X., Leon, L.J., Penkoske, P.A., Giles, W.R., Spano, M.L., Ditto, W.L., Winfree, A.T., 1998. Spatiotemporal evolution of ventricular fibrillation. Nature 392, 78–82.
Zhang, H., Iijima, K., Huang, J., Walcott, G.P., Rogers, J.M., 2016. Optical mapping of membrane potential and epicardial deformation in beating hearts. Biophysical J. 111, 438–451.